Lawrence Berkeley National Laboratory

Title
POLARIZATION OF RECOIL PROTONS IN PION-PROTON ELASTIC SCATTERING AT 532, 572, AND 689 MeV

Permalink
https://escholarship.org/uc/item/1sb5b13q

Author
Eandi, Richard D.

Publication Date
1963-03-18

University of California

Ernest O. Lawrence
Radiation Laboratory

POLARIZATION OF RECOIL PROTONS IN
PION-PROTON ELASTIC SCATTERING
AT 523, 572, AND 689 MeV

DISCLAIMER

UNIVERSITY OF CALIFORNIA

cy 3

Lawrence Radiation Laboratory
Berkeley, California

Contract No. W-7405-eng-48

ʟ

POLARIZATION OF RECOIL PROTONS IN PION-PROTON ELASTIC SCATTERING AT 523, 572, AND 689 MeV

Richard D. Eandi

(Thesis)

March 18, 1963

POLARIZATION OF RECOIL PROTONS IN PION-PROTON ELASTIC SCATTERING AT 523, 572, AND 689 MeV

Contents

POLARIZATION OF RECOIL PROTONS IN PION-PROTON ELASTIC SCATTERING AT 523, 572, AND 689 MeV

Richard D. Eandi

Lawrence Radiation Laboratory
University of California
Berkeley, California

March 18, 1963

ABSTRACT

Angular distributions of recoil-proton polarization for elastic scattering of positive and negative π mesons on protons were measured at 523, 572, and 689 MeV incident-pion kinetic energy. The pion source was an internal target of the Berkeley Bevatron. Polarization measurements were made by observing the azimuthal asymmetry of sample angular distributions of recoil protons which scatter in large carbon-plate spark chambers. The spark chambers proved to be very suitable polarization analyzer-detectors. The spark chambers were triggered by an array of scintillation and Cerenkov counters which identified the particles entering the chambers as recoil protons from elastic pion-proton scattering. Two plausible nonunique sets of phase shifts were obtained by employing: (a) restrictive assumptions related to the higher resonances, (b) available pion-proton total and differential cross sections measured at nearby energies, and (c) the measurements of this experiment. One set is characterized by a $J = 3/2$, $T = 1/2$, D-wave resonance; the other set is characterized by a $J = 3/2$, $T = 1/2$, P-wave resonance at 600-MeV incident-pion energy.

I. INTRODUCTION

Since the discovery of the pion in 1947, [1] the interaction between pions and nucleons has been widely studied, most often by pion-nucleon (πN) scattering and pion photoproduction experiments. With the advent of higher and higher energy pion beams, the π-N interaction was observed to be surprisingly complex. Both scattering and photoproduction cross sections showed a striking dependence on the energy of the incoming pion or photon. For example, if one looks at πN total cross sections as a function of incoming pion energy, one's attention is immediately drawn to the series of peaks of various widths and heights that occur. [2-4] A considerable amount of work has been done to interpret these maxima as resonances in definite quantum states of given angular momentum J, isotopic spin T, and parity ℓ. The first peak, occurring at about 200-MeV incident-pion kinetic energy, appears to be well understood in terms of a resonant interaction of meson and nucleon in a state of $J = 3/2$, $T = 3/2$, and even parity ($\ell = 1$). [5] Such phenomenological interpretation of the higher maxima at 600, 900, and 1350 MeV is less certain.

Some information has already been gained from measurements of the total cross sections and angular distributions in photoproduction and elastic scattering. The fact that the peaks at 600 and 900 MeV are observed in π^-p scattering and not seen in π^+p scattering is evidence that both maxima are due to an interaction in a definite isotopic spin state of $T = 1/2$. The relative behavior of the π^-p and π^+p total cross section at 1350 MeV indicates it to be in a 3/2 isotopic spin state.

The assignment of total angular momentum is based on the size of the total cross section and on analysis of the angular distributions in both elastic scattering and photoproduction. Near the 600-MeV peak, the angular distributions of photoproduced neutral pions is consistent with production in a state of $J = 3/2$. [6-8] The πN total and differential cross sections in π^-p scattering substantiate this assignment. [3, 9] Similarly, existing data indicate that the 900- and 1350-MeV "resonances" have total angular momenta of 5/2 and 7/2, respectively. [9, 10]

The assignment of parity to these maxima, assuming that they are single state resonances, is another matter. Due to the Minami ambiguity,[11] the parity of the state cannot be determined from angular distributions alone, although educated guesses can be made. Peierls,[8] in his analysis of pion photoproduction, suggested that the two T = 1/2 resonances at 600 and 900 MeV should be assigned parities corresponding to orbital angular momentum ℓ = 2 and 3, respectively. Although this assignment is not completely established there is no contradictory evidence. An experimental test of this conclusion was proposed by Sakurai.[12] He proposed that one make use of the fact that the nucleon that recoils when a photopion is produced is polarized if at least two angular momentum amplitudes with the proper phase relation interfere. Particularly, no polarization will be observed at 90 deg in the c.m. system unless two or more states of opposite parity are present. Experimentally, the recoil-proton polarization has been found to be quite large at energies intermediate between the 200- and 600-MeV peaks.[13,14] The assumption generally made is that this is due to an interference between an enhanced J = 3/2 state with odd parity and the tail of the well-known even parity, J = 3/2 resonance at 200 MeV. Polarization measurements have been carried out above the second maximum and show a rather large polarization at 90 deg c.m.[15] This is interpreted, following Peierls, by assuming that the 600- and 900-MeV peaks correspond to states of opposite parities.

So far, most parity assignments of resonances have been made with use of recoil-nucleon polarization in photoproduction. It is well known that the recoil nucleon from elastic πp scattering may be polarized even though the beam and target are not. As in photoproduction, this recoil-nucleon polarization can give useful clues to the parity assignments of these higher resonances, as well as verify the quantum numbers already assigned to them.[16,17] In fact, perhaps the situation in elastic scattering is even more favorable than in photoproduction because there are fewer states, since considerations are not complicated by photon multipoles. Measurements of the polarization, however, require high-intensity beams, so that few useful measurements

have been made. Due to the advent of better experimental techniques, polarization measurements in πp scattering are beginning to contribute to the store of knowledge of the πN interaction.[18]

In the final analysis the only really unambiguous way of verifying a resonance assignment would be a complete phase shift analysis (Appendix B) with a unique solution for scattering. At these high energies this becomes very difficult, due to the many partial-wave amplitudes that have to be included. The situation is further complicated by inelastic channels which make the phase shifts complex. In the absence of a unique way to verify assignments, therefore, one has to contend with plausibility and consistency arguments, such as those proposed by Peierls,[8] Moravcsik,[16] Sakurai,[12] and Shaw.[17]

In this experiment, carbon-plate spark chambers were used as a polarization analyzer in order to observe protons recoiling from a liquid-hydrogen target. The target was bombarded by a magnetically analyzed pion beam produced at the Berkeley Bevatron. The polarization of recoil protons as a function of pion scattering angle was measured at 523, 572, and 689 MeV for pions of both charge states (Fig. 1), in the hope of contributing significant independent information about both isotopic spin states of the πN system. These polarization angular distributions—in conjunction with elastic differential cross sections and total cross sections measured at nearby energies[10]—were used to investigate the 600-MeV maxima and to ascertain if it can indeed be interpreted as a resonance in a definite state.
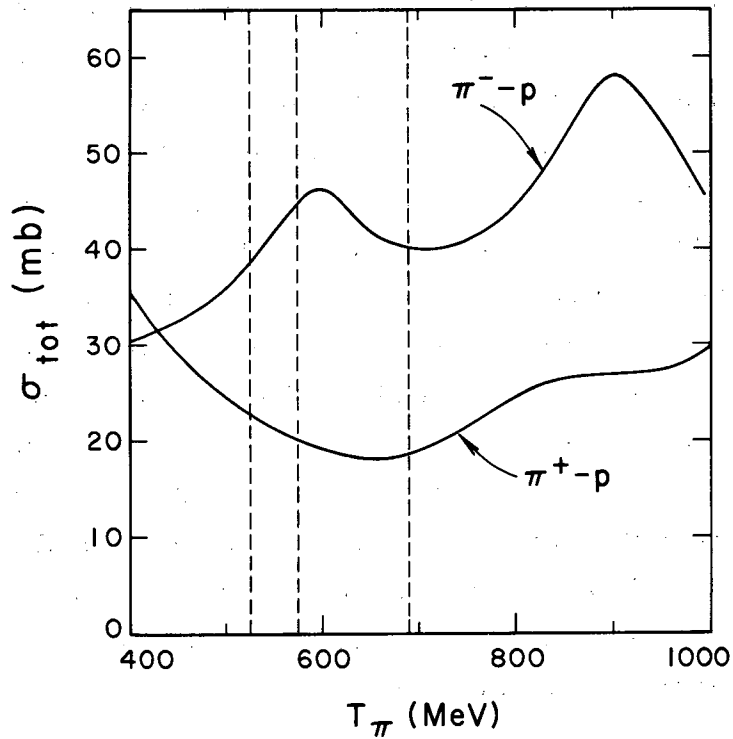
MU-29361

Fig. 1. Total cross sections for $\pi^\pm p$ scattering, showing the
energies at which the recoil-proton polarization was
measured in this experiment.

II. EXPERIMENTAL METHOD

A. General

A measurement of the polarization of the recoil proton requires a search for an azimuthal asymmetry in a subsequent scattering of the proton by a suitable polarization analyzer. From the conservation of parity in strong interactions, it can be shown that the proton polarization is perpendicular to the plane of scattering, defined by the recoil proton and the scattered pion momenta. The magnitude of the polarization P is determined from the angular distribution of the recoil protons scattered by the analyzer, according to the formula

$$\sigma(\theta, \phi, E) = \sigma_0(\theta, E)[1 + PA(\theta, E) \cos\phi],$$

where $A(\theta, E)$ is the analyzing power of the second scatterer for collisions in which protons of energy E are deflected through an angle θ, ϕ is the azimuthal angle between the plane of the first scatter and the plane of the second scatter (see Fig. 2), and $\sigma_0(\theta, E)$ is the cross section for unpolarized protons.

If the analyzing power A is known as a function of angle, energy, and energy resolution, there are at least two methods by which one can measure the magnitude of the polarization of the recoil protons:

1. A counter system can be set up to compare the counting rates for scattering at $\cos\phi = +1$ and $\cos\phi = -1$ for a given angle θ. This gives a direct measurement of the left-right asymmetry. However, pion beams of high intensity are necessary because of the double-scattering nature of the measurement and the typically small solid angle subtended by the two counters.

2. A visual detector (cloud chamber, emulsion, or spark chamber) can be used to obtain a sample of the angle distribution in both θ and ϕ of the proton scatters in the detection medium. The polarization may then be estimated from the sample by statistical analysis.

In this experiment the second method was applied. The limited intensity of the available pion beam (0.2 to 0.3 million pions per minute)
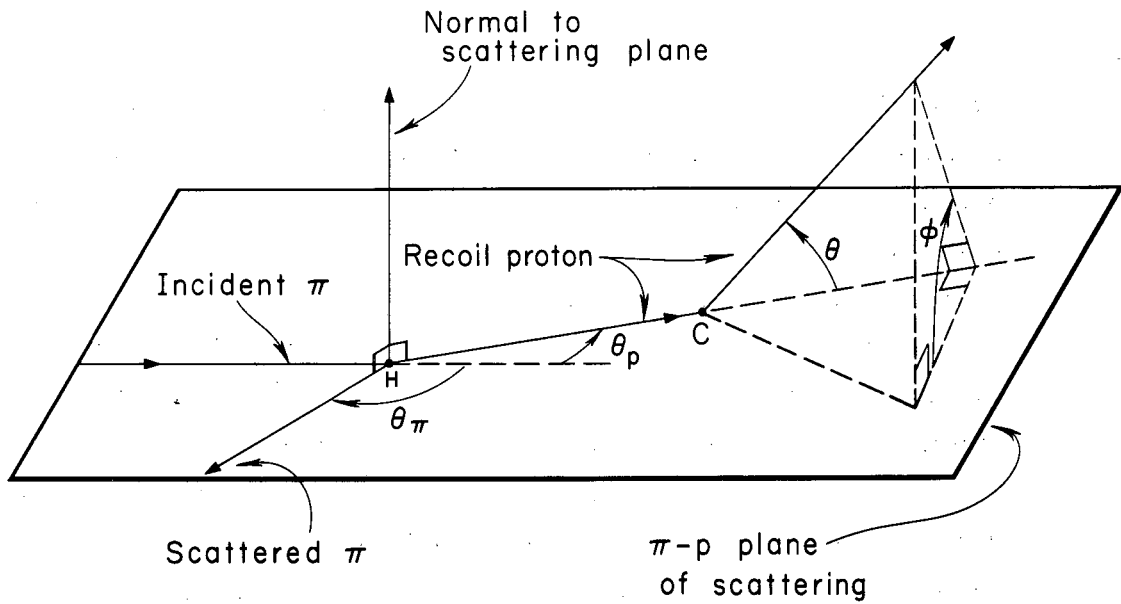
Fig. 2. A πp scattering event illustrating the recoil-proton re-
scattering off a carbon nucleus. All the kinematical
variables necessary in order to measure recoil-proton
polarization are defined in this diagram.

made it very desirable to use a "long" hydrogen target to increase the interaction rate. This was made possible by use of large carbon-plate spark chambers as detector-analyzers. Their high angular resolution and wide acceptance enabled us to use a long hydrogen target without loss of πp scattering-angle information. Because of the strong variation of $A(E, \theta)$ with proton energy and scattering angle, their energy resolution (track-length measurements) were also needed. The recoil-proton polarization of many different angles of pion scattering could be measured simultaneously because of their large sensitive volume. The use of these spark chambers also gave us the advantage of preselecting an event before deciding to detect it. This was accomplished by triggering the spark chambers with an array of scintillation and Cerenkov counters which identified the particle entering the chambers as recoil protons from elastic πp scattering. The resulting experimental setup is shown in Fig. 3.

B. Pion Beam

The pions were produced by bombarding an aluminum oxide ceramic target with the pulsed circulating beam of protons in the Bevatron. This target material was chosen as a compromise between minimizing the electron contamination (by using low-Z material) and maximizing pion production (by using high-density material).

The pions traversed the apparatus of another experiment,[19] for which they were brought to a focus at T_1, and were refocused by means of a quadrupole to form the desired beam, shown in Fig. 4. The central momentum and momentum spread of the beam were determined by the magnetic beam-transport system of this upstream experiment. The momentum band, $\Delta P/P$, was ± 3%. The beam intensity was approximately 30 000 pions per Bevatron pulse. The pion pulse length in time was 200 msec, and a pulse was produced every 6 sec during the experiment.

The quadrupole was operated to give a vertical focus 2 ft behind the hydrogen target, and a horizontal focus at the center of the target flask. These focal conditions ensured the optimum use of the
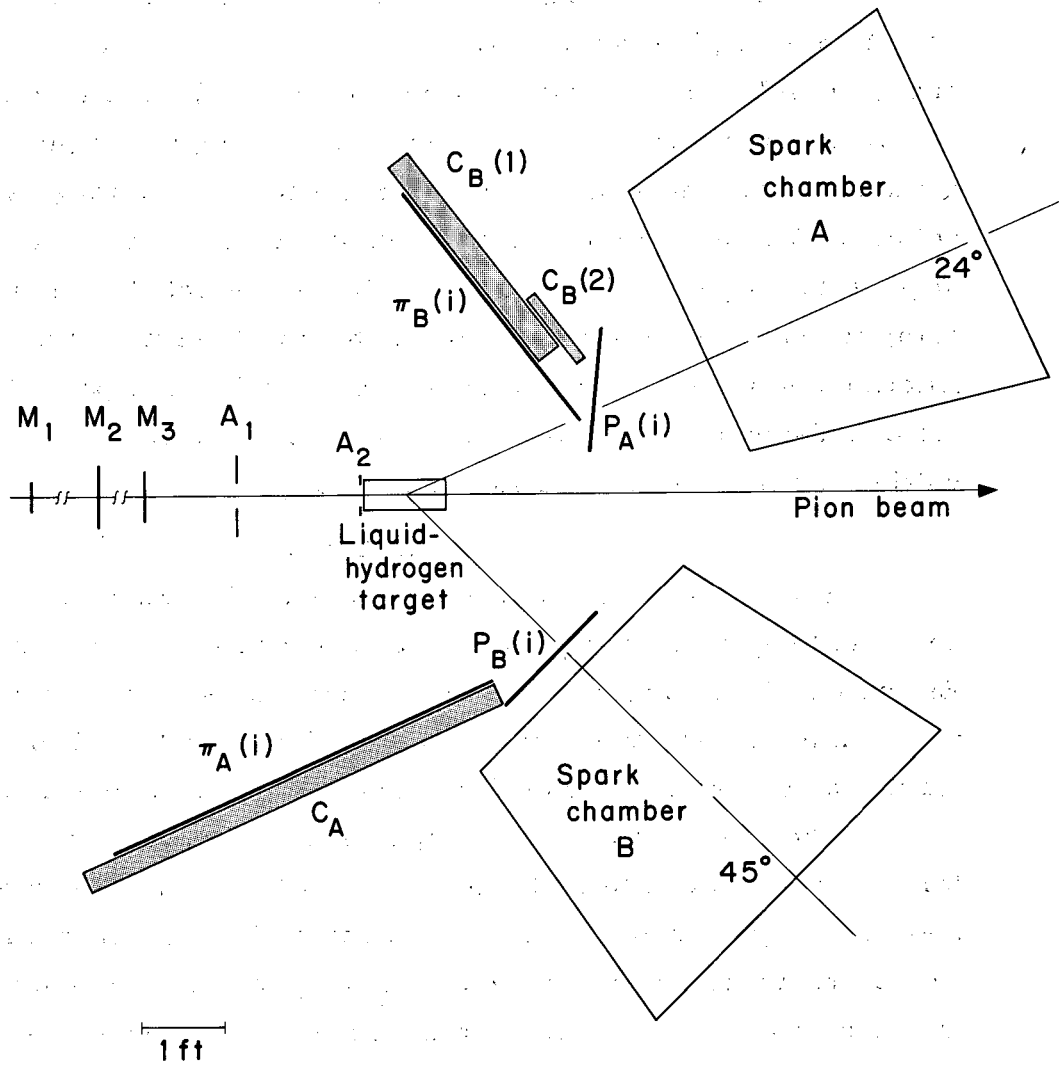
Fig. 3. Plan view of this experiment, showing the orientation of spark chambers and counters used to select desired events.
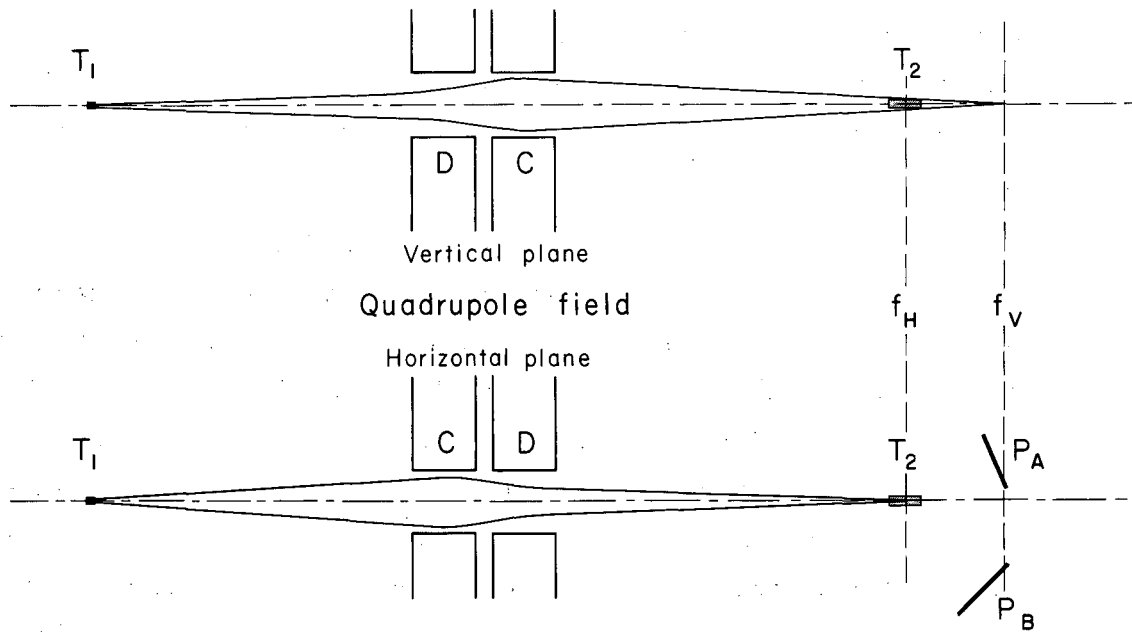
MUB-1614

Fig. 4. Beam optics diagram.

C = convergent quadrupole element

D = divergent quadrupole element

T_1 = hydrogen target of another experiment

T_2 = hydrogen target of this experiment

f_H = horizontal beam focus

f_V = vertical beam focus

P_A = proton counters for spark chamber A

P_B = proton counters for spark chamber B.

coplanarity condition for elastic πp scattering. To have good co-planarity the plane-defining counters must be far enough away from the finite-sized target to satisfactorily define a plane. In order to minimize the detection of inelastic (noncoplanar) events, the vertical width (plane-defining dimension) of these counters must be minimized. But this width should never be smaller than the vertical width of the pion beam seen by these counters if one does not wish to lose counting efficiency. Since the scattering planes defined by each πp elastic event all intersect at the vertical focus, the vertical dispersion of the scat-tered particles is a minimum at this focal position. The nearer the counters are to this vertical focus, the smaller their vertical width. The proton counters were chosen to fulfill this condition. Thus the vertical focus was placed at the ends of the proton counters as shown in Fig. 4.

C. Liquid-Hydrogen Target

The two main components of the liquid-hydrogen target are shown in Fig. 5. The flask and vacuum jacket were constructed with one purpose in mind: to virtually eliminate the possibility of detecting an event in which the pion did not scatter in liquid hydrogen. This was accomplished in a twofold manner: by keeping the amount of structural material exposed to the beam to a bare minimum within the limits of safety, and by installing a scintillation counter within the vacuum jacket in order to electronically eliminate pions which could scatter off the flask walls. In addition, since the density of liquid hydrogen is so low, the target was made long enough to obtain a counting rate compatible with our data-collection rate capability.

With this in mind, we constructed the vacuum jacket from a 5-1/2-in.-diam aluminum cylinder with a spun-aluminum dome on one end, both of whose walls were 0.031 in. The front end had a 0.015-in. Mylar window. The liquid-hydrogen flask itself was a 4-1/2-in.-diam 12-in.-long cylinder with 0.010-in. Mylar walls. The end domes of the flask were also made of 0.010-in. Mylar. The hydrogen fill-line, protruding down to the bottom of the flask, was a 1/2-in.-diam Mylar tube with 0.005-in. walls.

Housing for
scintillation
counter, A_2

Boil-off

To
liquid-hydrogen
reservoir

Scintillation
counter, A_2

Liquid-hydrogen flask

Aluminum vacuum jacket
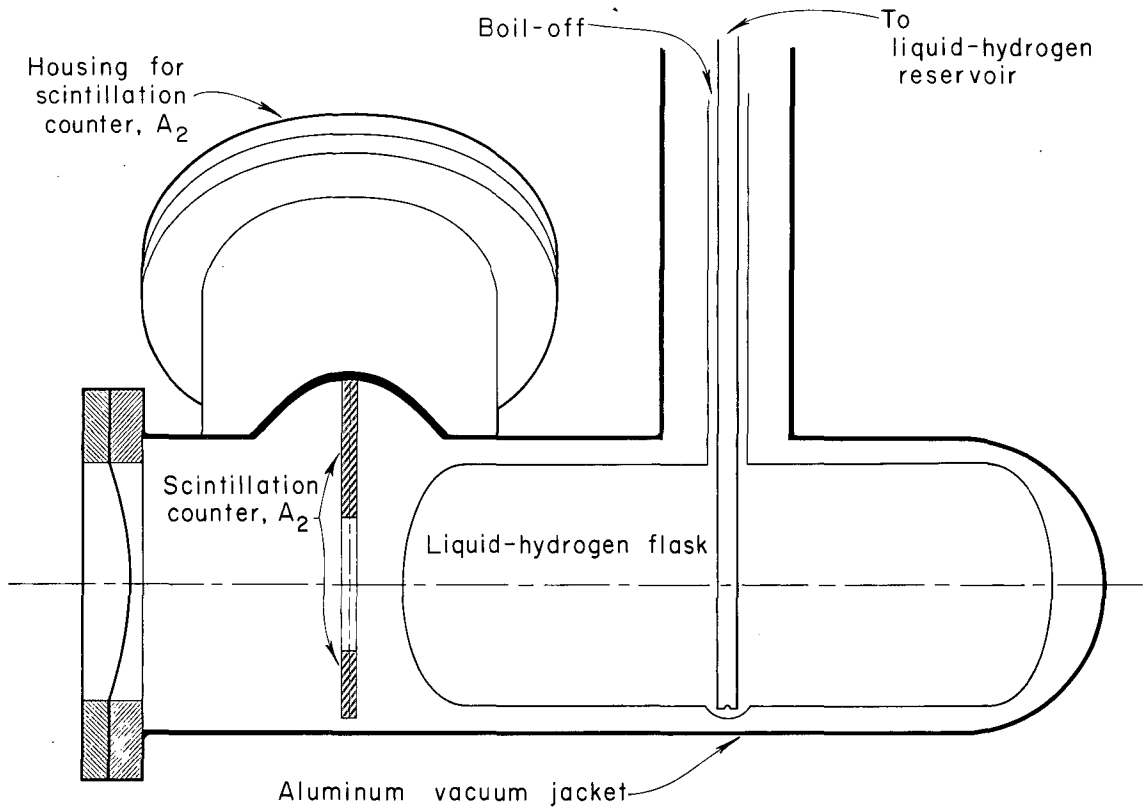
MUB-1615

Fig. 5. Liquid-hydrogen target and internal beam-defining
scintillation counter.

D. Counters

The selection of events to trigger the spark chambers A and B was accomplished by a system of plastic scintillation counters and water Cerenkov counters, arranged as in Fig. 3.

The pion beam was monitored by counters M_1, M_2, M_3 before entering the liquid-hydrogen target. An annular counter, A_1, had an inner and outer diameter chosen to prevent the selection of any scattering event whose incident pion traversed the material of the vacuum jacket surrounding the hydrogen flask. Another annular counter, A_2, was installed within the vacuum jacket in order to eliminate the counting of any pion that could possible simulate an event by impinging on the cylindrical Mylar walls of the flask itself (see Fig. 5). These two counters, when electronically added together, certified that the incident pion of virtually all the events selected traversed only the liquid-hydrogen target. The description of the above-mentioned counters is given in Table I.

Table I. Details of beam-defining counters.

Counter	Type	Shape	Dimensions (in.)	Phototube type
M_1	Scint.	Rectangular	4-1/2 × 2-1/2 × 1/4	RCA 6810A
M_2	Scint.	Rectangular	6 × 8-1/2 × 1/4	RCA 6810A
M_4	Scint.	Disk	7 diam × 1/8 thick	RCA 6810A
A_1	Scint.	Annular	4 (i. d.) × 12 (o. d.) × 1/4	RCA 6810A
A_2	Scint.	Annular	3-1/2 (i. d.) × 5 (o. d.) × 1/4	RCA 6810A

Each spark chamber had four identical channels (although only one can be illustrated in Fig. 3), each consisting of a pion counter $\pi(i)$, a proton counter $p(i)$ ($i = 1, 2, 3, 4$), and a water Cerenkov counter C, which all four channels had in common. The dimensions of the counters are given in Table II. These counters were shaped to approximate sections on the surface of a sphere centered at the hydrogen target. The pion and proton counters comprising a given channel i subtended an azimuthal angle increment, $\Delta\phi$, of 1/12 rad, where ϕ is the azimuthal

angle in the spherical coordinate system with the beam as the polar axis. The purpose of the counters was to select elastic-scattering events by imposing the condition that the event be coplanar. The planes, defined by each proton and pion counter of a given channel, were azimuthally separated by $1/12$ rad in ϕ, so that the total azimuthal angle subtended by all four channels was $1/3$ rad. To ensure that only protons entered the chambers, the scattered pion was detected by a water Cerenkov counter which would not respond to protons. The kinematically conjugate counter was then assumed to count the recoil proton. Recoil protons that scattered from the hydrogen target with their polar angle between 13 and 40 deg were detected by chamber A, while chamber B detected those whose polar angle ranged between 32 and 65 deg.

The orientation of the spark chambers, all the proton and pion counters, and the Cerenkov counter for chamber A remained fixed with respect to the hydrogen target for all three of the beam energies used. The pion counters were made long enough to account for the kinematical shifting of the scattered-pion direction for a fixed recoil-proton direction when the beam energy was changed.

Unfortunately, πN kinematics required that the proton counters $p_A(i)$ and the pion counters $\pi_B(i)$ overlap at the highest energy, 689 MeV. This made it necessary to place the Cerenkov counter for spark chamber B in the path of the protons traversing the proton counters for spark chamber A (see Fig. 3). This was remedied by making the Cerenkov system for spark chamber B consist of two Cerenkov counters $C_B(i)$, $i = 1, 2$, whose signals were electronically added. The smaller one $C_B(2)$ overlapping the proton counters was constructed as thin as possible to minimize the amount of scattering material in the path of the protons entering spark chamber A. For the lower two energies, where there was no overlapping, $C_B(2)$ was removed. This problem did not occur for spark chamber B since the kinematics required no interference between the Cerenkov counter C_A and the proton counters $p_B(i)$.

Table II. Details of counters for elastic-scattering detection.

Counter	No.	Type	Dimensions[a] (in.)	Phototube type and No.
$\pi_A(i)$	4	Scintillator	60×(4-1/2×2-1/2) ×1/2	1-RCA 6810A each
$P_A(i)$	4	Scintillator	18×(2×1/2)×1/4	1-RCA 6810A each
C_A	1	H_2O Cerenkov	65×(20×12)×3-1/2	3-RCA 7046
$\pi_B(i)$	4	Scintillator	42×(3-1/2×1)×1/2	1-RCA 6810A each
$P_B(i)$	4	Scintillator	19×(2-1/2×1-1/2) ×1/4	1-RCA 6810A each
C_B	2	H_2O Cerenkov	36×(16×10)×3-1/2	2-RCA 7046
			14×(12×12)×1-1/2	1-RCA 7046

[a]Since counters are regular trapezoids in shape, the following convention is used to give counter dimensions: $L \times (W_1 \times W_2) \times T$, where
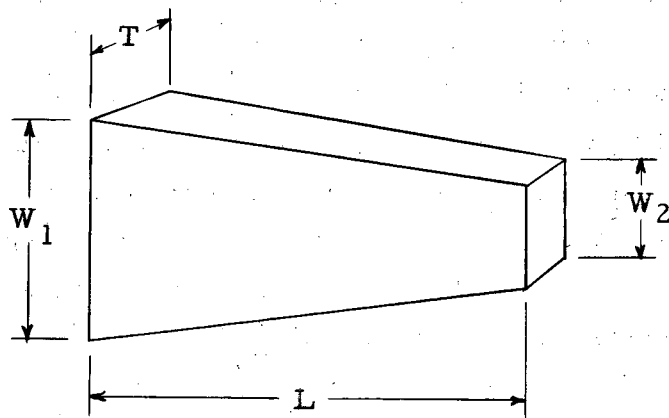
All the plastic scintillation counters were made of a solution of terphenyl in polystyrene. The scintillators were viewed through lucite light pipes by photomultiplier tubes. All three water Cerenkov counters were constructed by filling reinforced lucite tanks with water. Amino-G-acid was used as wavelength shifter. Air light pipes made of highly polished aluminum sheet were used to collect the Cerenkov light. Table II shows the type and number of photomultiplier tubes used for each counter. Counter C_A had a measured efficiency for detecting pions of greater than 80%. The detection efficiency of both $C_B(1)$ and $C_B(2)$ was greater than 85%.

The fact that the Cerenkov detection efficiences are less than 100% or that they may depend on the incident-pion energy affects only our ability to gather events, since the spark chamber is not triggered unless a Cerenkov signal indicating the traversal of a pion is received by the electronics system (see Sec. II. E.).

E. Electronics

The electronics system for this experiment is shown in Fig. 6. All the coincidence circuits, amplifiers, discriminators, signal splitters and mixers are standard units used at the Lawrence Radiation Laboratory. Descriptions of all these circuits may be found in the LRL Counting Handbook.[20]

The logic used to trigger each chamber is identical. The functions of each coincidence circuit are:

1. The M circuit ensured that the pion was properly momentum analyzed by the magnetic beam-transport system and that it only traversed the liquid hydrogen in the flask. This circuit also rejected, by time of flight, the protons contaminating the positive-pion beam.

2. The C circuit certified that a pion and not a proton scattered into the proper Cerenkov counter.

3. The No. i circuit (i = 1, 2, 3, 4) took the output signal from the C circuit and required that a coincidence occur between this signal, the pion counter $\pi(i)$, and the conjugate proton counter $p(i)$.
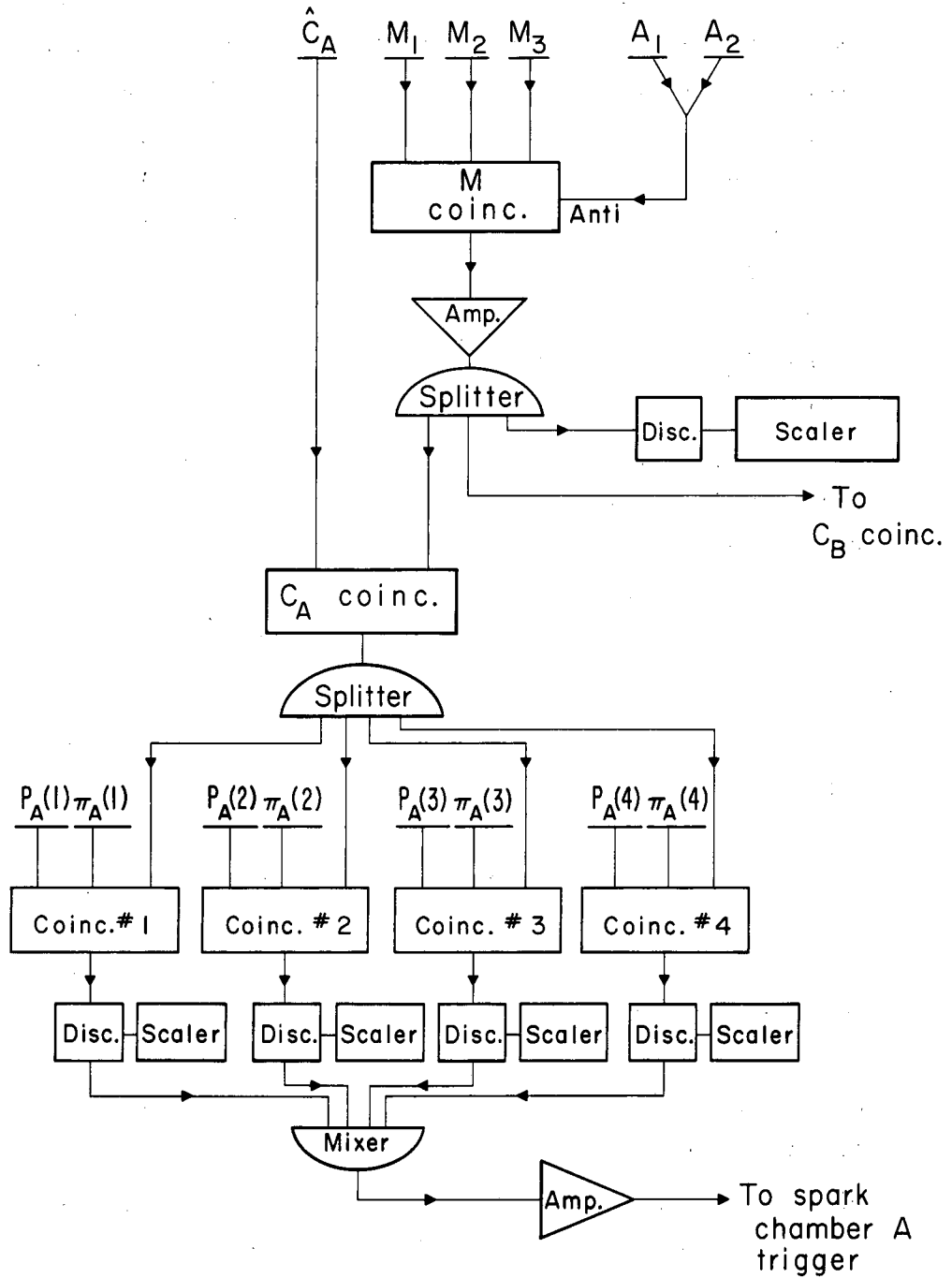
Fig. 6. Block diagram of electronics, drawn as a flow diagram showing the logic used to trigger the spark chambers.

The outputs from these circuits were then added and fed to the spark-chamber triggering system shown in Fig. 7.

Thus the selection of an event to trigger a chamber, A or B, required the following coincidence equation to be satisfied:

$$\text{event} = M_1 + M_2 + M_3 + C - (A_1 + A_2) + \sum_{i}^{4} [p(i) + \pi(i)]$$

where a "+" means coincidence and a "-" means anticoincidence.

F. Spark Chambers

To make optimum use of beam, two spark chambers[21,22] were constructed large enough to measure simultaneously the polarization of recoil protons for all physically accessible proton angles. Each chamber consisted of thirty-five 1-in. plates ranging in dimensions from 44×20 in. for the front plate to $58-1/2 \times 23-1/2$ in. for the back plate. The gap width between plates was 1/4 in. In order to define the direction of the particle incident on a chamber before a carbon interaction, three "massless" plates, made by stretching 0.003-in. aluminum foil over $44 \times 20 \times 1$-in. open frames, were placed at the incident end of each chamber. In addition spark chamber B, looking at the lower-energy recoil protons, had partially hollow plates. Five of its plates had only 1/4-in. carbon slabs on one side of an open frame and 0.003-in. aluminum foil on the other. Its next five plates contained 1/4-in. carbon slabs on both sides of the frame, leaving a 1/2-in. hollow spacing in the center. In this way the gaps remained 1 in. apart, resulting in better spatial resolution from the large spark separation. Figure 8 shows one of the carbon-plate spark chambers being built.

With chamber B it was possible to stop protons that had energies up to 450 MeV, at their origin in the hydrogen target. Spark chamber A, looking at the higher-energy protons, stopped protons of up to 530 MeV. Thus both chambers revealed knowledge of the energy of the proton in addition to giving good probability of scattering and angular information.

Both spark chambers were being filled continuously at atmospheric pressure with a mixture of 98% welder's argon and 2% alcohol, and were completely flushed out with Argon every few hours to eliminate
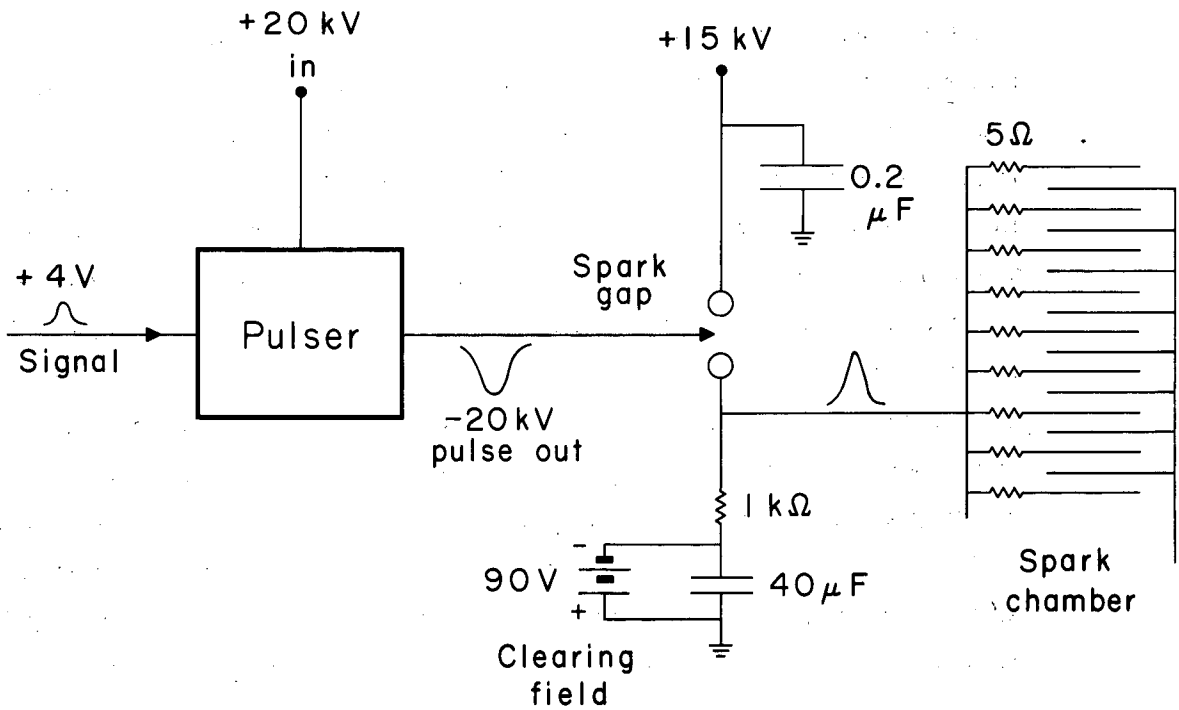
Fig. 7. System used to fire the spark chambers on a given
signal from the counter electronics.
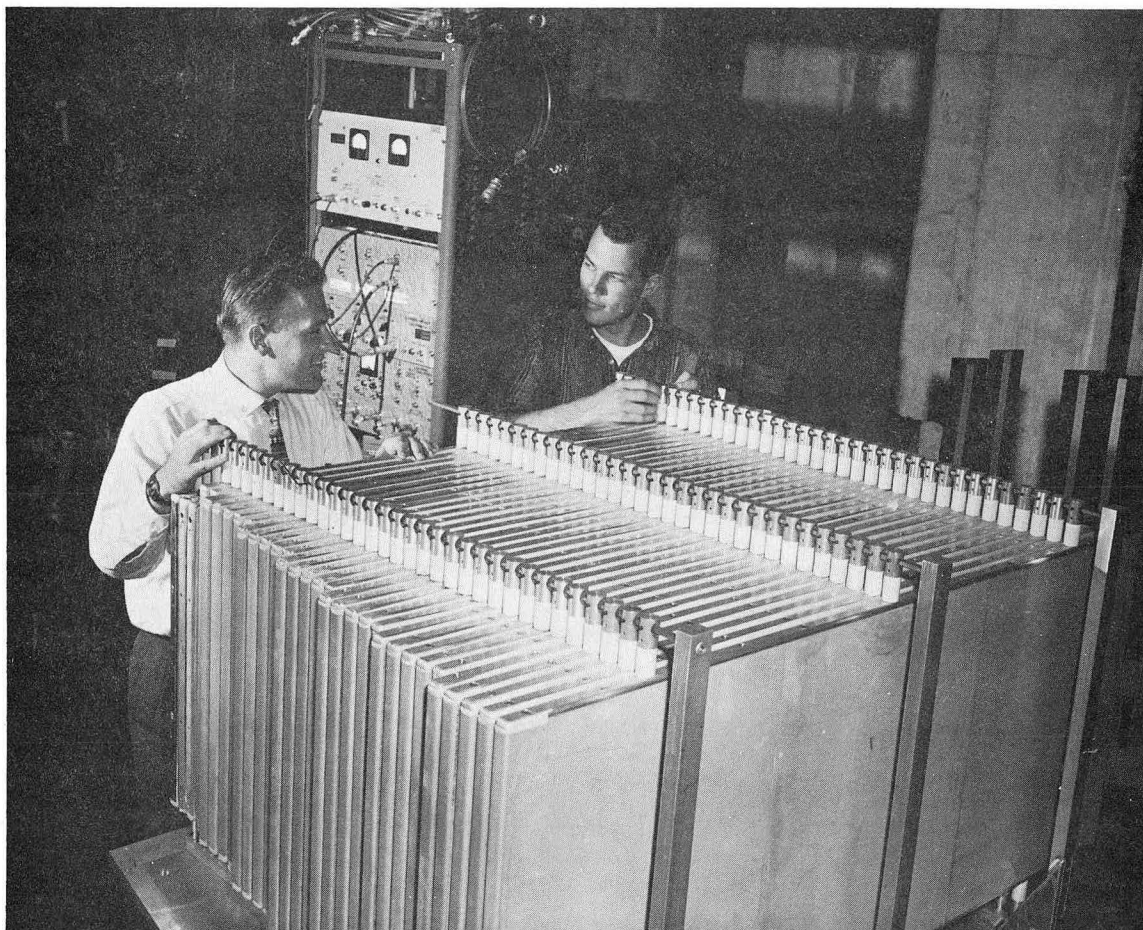
ZN-3634

Fig. 8. One of the carbon-plate spark chambers used in this experiment.

contaminants produced from sparking. Under these conditions the gap efficiency, (the probability that a gap fires when it should) was always greater than 95%.

The system for firing each spark chamber is shown schematically in Fig. 7. Upon receiving a signal from the counter electronics, a pulser[23] put a negative 20-kV pulse on the triggering needle of a spark gap. When the spark gap discharged, it placed a pulsed voltage of 15 kV on alternate plates of the spark chamber. A clearing field of up to 50 V was used, with opposite polarity.

G. Background

The selection of events other than elastic πp scattering was minimized by the multi-coincidence requirements and the stringent application of the coplanarity condition. The effect of the inelastic background, (i. e., pion scattering with the production of an additional pion) was made insignificant by imposing range requirements on the recoil proton consistent with kinematics for elastic scattering. (This is disucssed in Sec. III. B.)

The scattering of pions on material other than liquid hydrogen was very small. The ratio of the target-full to target-empty counting rate was 25 or greater at all three beam energies. Upon scanning the target-empty film it was found that practically all the tracks recorded possessed entrance directions clearly not originating at the hydrogen flask. The effect of this background was all but eliminated by requiring that the particle track—addition to range requirements—must have its origin in the liquid-hydrogen flask when projected back along its direction of flight.

H. Photography

Figure 9 shows the optical system for each spark chamber. Each chamber used two large plano-convex lucite field lenses in order to obtain two 90-deg stereo views of every event. The curved surfaces of the lenses were made slightly hyperboloidal in order to eliminate spherical aberration. The focal length of the top-view lens was 15.5 ft. For the side-view lens the focal length was 19.5 ft, due to longer optical
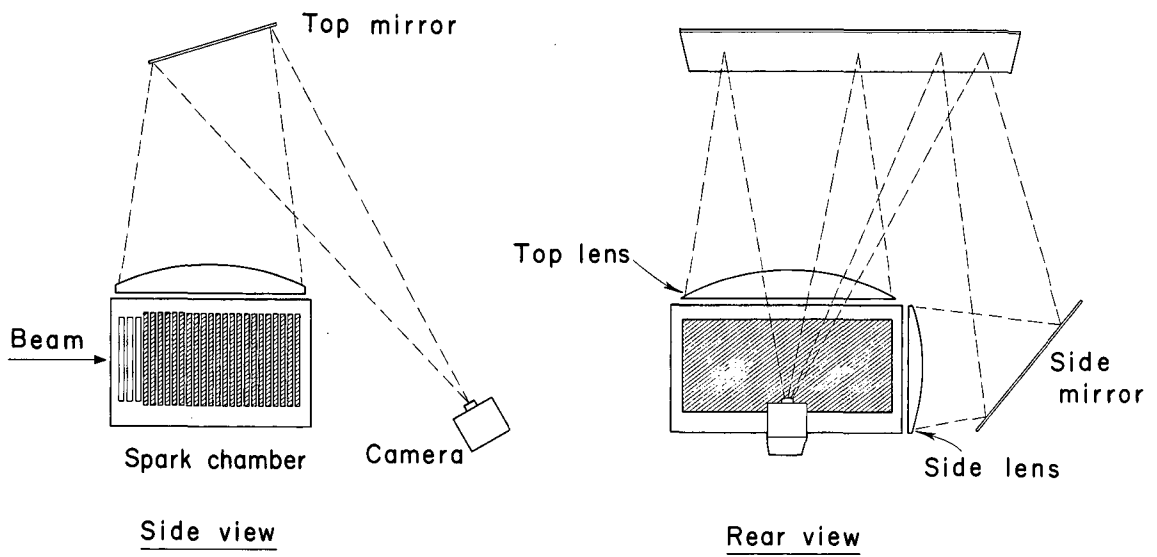
Fig. 9. Diagram of spark-chamber optics used to photograph the selected proton events.

path from lens to camera. A system of two plane front-surfaced mirrors projected the two stereo views into a single camera. The camera was placed at an optical distance consistent with the focal lengths of both the side and top lenses. The camera lens was set at f/16. Panatomic-S film was used; it was advanced every six seconds between Bevatron beam pulses.

A reference coordinate system was produced by scribing an orthogonal grid array on the top and side windows of each chamber. These grids were illuminated by piping light into the ends of the lucite windows (see Fig. 10). This permitted the correction of measuring errors produced by lens distortion when the film was reprojected for scanning.
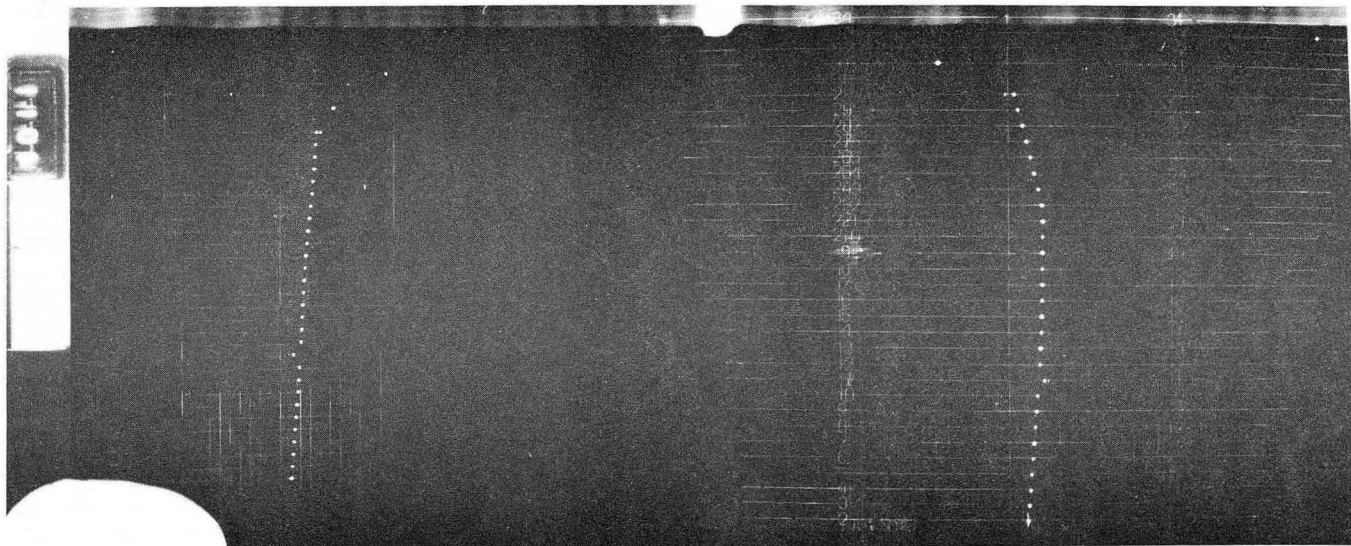
ZN-3633

Fig. 10.   Photograph of an event.   The smaller view on the left
            is the side view of the proton spark chamber with protons
            entering from the bottom of the figure.   On the right is
            the top view of the chamber.

III. DATA ANALYSIS

The calculation of the polarization of recoil protons scattering into a given angular interval was performed in two steps:

First, the spark-chamber film was scanned and each selected scatter was geometrically and kinematically reconstructed.

Second, for a given sample of events, the effective analyzing power, $A(E, \theta) \cos \phi$, was calculated for each p-C scatter.

The polarization was then estimated from this sample by a statistical method of analysis known as the maximum likelihood method. These steps are described in detail below.

A. Scanning

During this experiment 270 000 photographs were taken, one photograph per spark chamber per Bevatron beam pulse. Each photograph consisted of two orthogonal views of a chamber, and recorded from zero to three proton tracks.

A group of scanners viewed these pictures and measured events suitable for polarization analysis. The measurement of an event consisted of recording the recoil-proton entrance position, the proton entrance angle, the proton-carbon scattering angle and sense, the number of plates traversed by the proton before scattering, and total number of plates penetrated, for each of the two views. Any event that did not meet the criteria below was not measured and was rejected:

1. Each proton's projected entrance angles were required to be within certain angular limits determined by target size and location. This eliminated events that obviously did not originate in the liquid-hydrogen target.

2. Each proton was required to scatter only once.

3. Each proton was required to show a distinct scattering vertex by having at least three sparks in a straight line on either side of the vertex. This ensured a reliable angle measurement.

4. Each proton was required to have a proton-carbon scattering angle between 4 and 25 deg in the top view, and between 0 and

25 deg in the side view. This reduced the inclusion of events due to Coulomb scatterings and inelastic scatterings.

5. Each proton was required to stop in the chamber.

6. Each proton was required to have stayed in the chamber if it had scattered in the other direction. This eliminated up-down and left-right biases in event selection.

In addition, any track that had too many missing sparks was disregarded. In photographs containing more than one track, if any ambiguity at all arose in matching the top and side views of a track the event was rejected. For each accepted event, the proton's projected entrance angles were measured by using the sparks between the three front "massless" plates. This was done to eliminate errors in proton entrance direction caused by Coulomb scattering in the plates before the scattering vertex. Table III gives the number of events satisfying the above criteria, along with total pictures taken per energy and pion charge.

Table III. Number of events detected in spark-chamber scan.

Energy (MeV)	Pion charge	No. pictures	No. Events
523	+	56 000	1914
523	-	56 000	2342
572	+	36 000	1694
572	-	42 000	1831
689	+	46 000	2218
689	-	36·000	2338

B. Data Reduction I

An IBM 709-7090 FORTRAN computer program was written to calculate, for each event measured, the following parameters necessary for the further classifying and sorting of these events.

1. The proton's recoil angle θ_p and the cosine of the c.m. scattering angle of its corresponding pion, $\cos \theta_\pi^*$, were computed for each event. From the recoil-proton's entrance angle it was determined whether the proton originated in the hydrogen flask. Any event which did not was given a code number by the computer and later sorted out and rejected. Events were sorted later according to $\cos \theta_\pi^*$, enabling the calculation of the polarization as a function of pion scattering angle.

2. The kinetic energy of the proton when scattering off carbon was computed from the residual range of the proton after scattering, by using the known range-energy relations.[24] The kinetic energy of the recoil proton T was calculated in two ways: (a) T_r is the energy of the proton calculated by total range, and taking into account the recoil loss in p-C scattering; (b) T_k is the energy calculated by using the incident-pion energy and recoil-proton angle, assuming elasticity of the πp scattering. We calculated an uncertainty ΔT_k, which is due to incident-pion momentum spread ($\pm 3\%$), the horizontal divergence of the incident beam (± 1.5 deg), and error in angle measurement (± 1 deg). Also, we calculated an uncertainty ΔT_r corresponding to half the width of a carbon plate (± 2.2 g/cm^3). Then T_k and T_r were compared and if $|T_k - T_r|/\Delta T \leq 1$, where $\Delta T = [(\Delta T_k)^2 + (\Delta T_r)^2]^{1/2}$, the event was accepted; if not, the event was rejected as being an inelastic event.

Depending on the incident energy and entrance angle, ΔT ranged from 20 to 50 MeV. (This inability to resolve the proton's energy any better and its consequences are discussed in Sec. III. E.)

3. For protons whose entrance angles are not normal to the carbon plates, the number of sparks after the scatter will differ for a left scatter and a right scatter. This is due to the difference in the carbon-per-plate traversed. Thus our minimum three-sparks scanning

criterion may introduce a left-right bias by accepting, say, a left scatter whose residual range is three sparks but whose mirror image right scatter would have been rejected for having less than three sparks. The computer program calculated whether three sparks would be possible for both right and left scattering, and gave a corresponding code number to the event. The events were later sorted on this code number and rejected.

Table IV shows the number of events remaining for each energy and charge after sorting out all events that did not fulfill the above conditions.

Table IV. Number of surviving events per energy and charge.

Energy (MeV)	Pion charge	No. valid events
523	+	1160
523	-	1497
572	+	1170
572	-	1151
689	+	1089
689	-	1181

The events of a given pion incident energy and charge were then sorted and ordered as a function of $\cos \theta_\pi^*$. They were then grouped in angular bins of width $\Delta \cos \theta_\pi^* = 0.1$ and were available for polarization calculations by the method described in the following section.

C. Statistical Analysis

To estimate the polarization of a group of protons in a given angular bin, one may simply compare the number of scatterings to the left and right then divide the computed asymmetry by a suitably constructed average of the analyzing power over the chosen interval in angle and energy. This procedure, while simple, has several disadvantages. The scattering distribution depends on three variables: the scattering angle θ, the azimuthal angle ϕ, and the energy of the

protons at the point of scattering, E. These three variables vary appreciably and are all measured for each scattering event. The averaging over all of these three variables produces a loss of information that one cannot afford if the statistical sample is small. Furthermore, in order to construct an average analyzing power, an integration must be performed over the three-dimensional distribution—which must include the effects of the detection efficiency as a function of these variables, and event location in the spark chamber.

These complications can be circumvented by use of the maximum likelihood method. This method has three advantages: (1) the estimate obtained is statistically optimum, in the sense that the distribution of the estimates obtained from successive independent samples has minimum variance; (2) the information obtained in measuring the polar and azimuthal angles and energy of each event is not lost, or incorrectly averaged over, but it is all properly weighted; (3) the p-C differential cross section and scanning efficiency need not be known, although the efficiency must be unbiased.

For a formal discussion of the maximum likelihood method the reader is referred to Appendix C.

For present purposes the maximum likelihood method can be described as follows. For a sample of protons having a polarization P the probability of a scattering occurring at a given polar angle θ, azimuthal angle ϕ, and energy E is

$$P(\theta, \phi, E)d\Omega = \frac{1}{N} \sigma(\theta, E) [1 + PA(E, \theta) \cos \phi]. \tag{1}$$

The normalizing factor N is obtained by integrating the above equation over all solid angles. (Note that since the integration over ϕ is symmetrical about $\phi = \frac{\pi}{2}$, the polarization, which is unknown here, is not involved as a parameter in the normalization factor N.) For a given P, the total probability L for the occurrence of all the measured events in the sample will be the product of the individual probabilities for these events. The maximum likelihood theorem states that the actual recoil-proton polarization is that value of P that makes this product a maximum. This is equivalent to stating that the value of P is the

value which allows the observed array of events to be consistent with maximum probability. Thus one has to maximize the expression

$$L = \prod_{i}^{N} [1 + PA(\theta_i E_i) \cos \phi_i]$$

with respect to P. The product of the normalization factor and cross section can be omitted since they are independent of P. The statistical error is arbitrarily defined as that increment of P which makes L/L_{max} equal to $e^{-1/2}$ (see Appendix C).

D. Data Reduction II

A second IBM 709-7090 computer program was written to determine the effective analyzing power $A(E, \theta) \cos \phi$ for each event in a given angular interval of $\cos \theta_\pi^*$, and then to compute the likelihood function as a function of polarization P. At this point, I would like to define two terms which will be used repeatedly in this section. I shall call $A(E, \theta) \cos \phi$ the analyzing power of carbon for determining the polarization of incident protons. The quantity $A(E, \theta)$, by itself, I shall refer to as the analyzability for protons on carbon.

The analyzability $A(E, \theta)$ corresponding to p-C scattering was obtained from data furnished by V. Z. Peterson.[25] These data are reproduced in Figs. 11, 12, and 13. These graphs were approximated by tables that were fed into the computer memory to be used at the program's command. The value of the analyzability for each event was found by linear interpolation from these tables. The variables $\theta(E/180 \text{ MeV})^{1/2}$ and A/A_{max} were chosen in order to factor out the rapid variation of A with energy and angle, thus giving the linear interpolation process more precision. The quantity A_{max} is the peak analyzability that carbon can have for a proton of given energy.[25] The relatively smooth behavior of the contour graphs (Figs. 11 and 12) bears out this assumption.

Two different analyzability tables were used: the first assumed all p-C scattering events were elastic; the second included inelastic p-C scatterings up to 30 MeV energy loss (see Sec. III. E. 2).
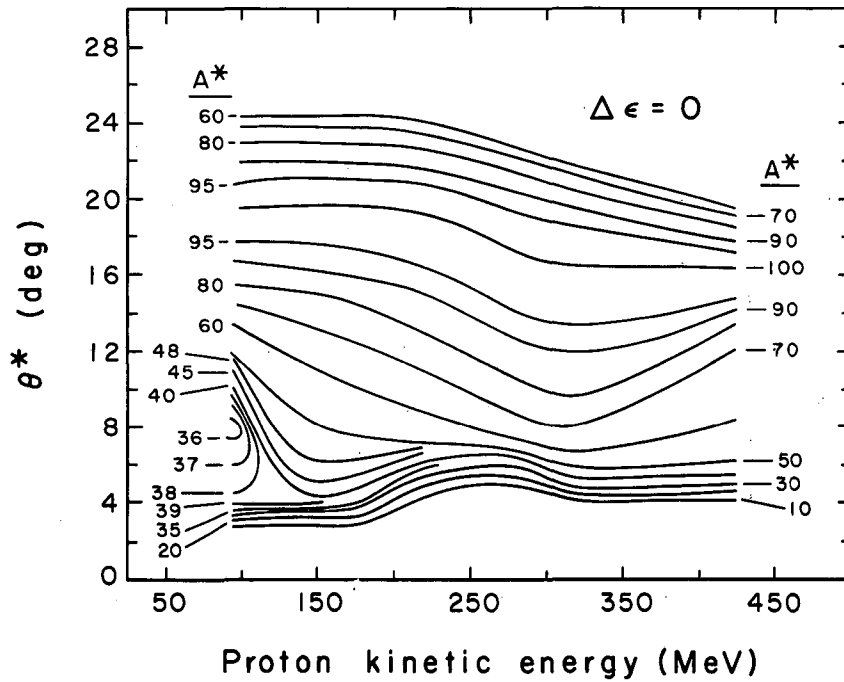
MU-29522-A

Fig. 11. Curves of constant A^* for elastic scattering ($\Delta\epsilon = 0$) of protons from carbon as a function of laboratory-system energy and θ^*, where θ^* and A^* are related to laboratory scattering angle (θ_{lab}) and analyzability A by

$$\theta^* = \theta_L (E/180 \text{ MeV})^{1/2} \text{ and } A^* = (A/A_{max}).$$

A_{max} is given in Fig. 13; E is energy of incident proton.
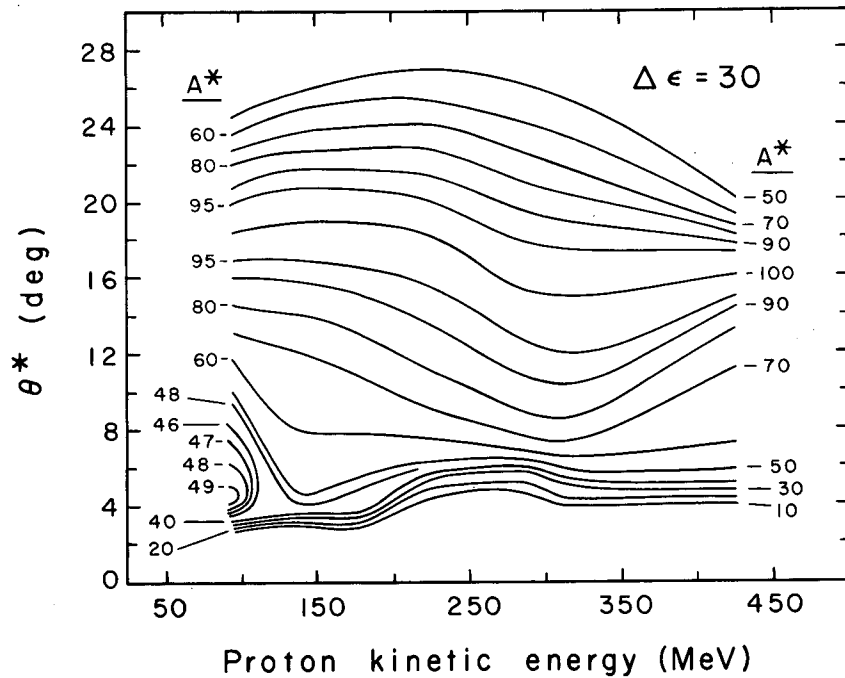
MU-29521-A

Fig. 12. Curves of constant A^* for p-C scattering, including inelastic scatterings up to 30 MeV ($\Delta\epsilon$ = 30 MeV), as a function of laboratory-system energy and θ^*, where θ^* and A^* are related to laboratory scattering angle θ_L and analyzability A by

$$\theta^* = \theta_L (E/180 \text{ MeV})^{1/2} \text{ and } A^* = A/A_{max}.$$

A_{max} is given in Fig. 13; E is energy of incident proton.
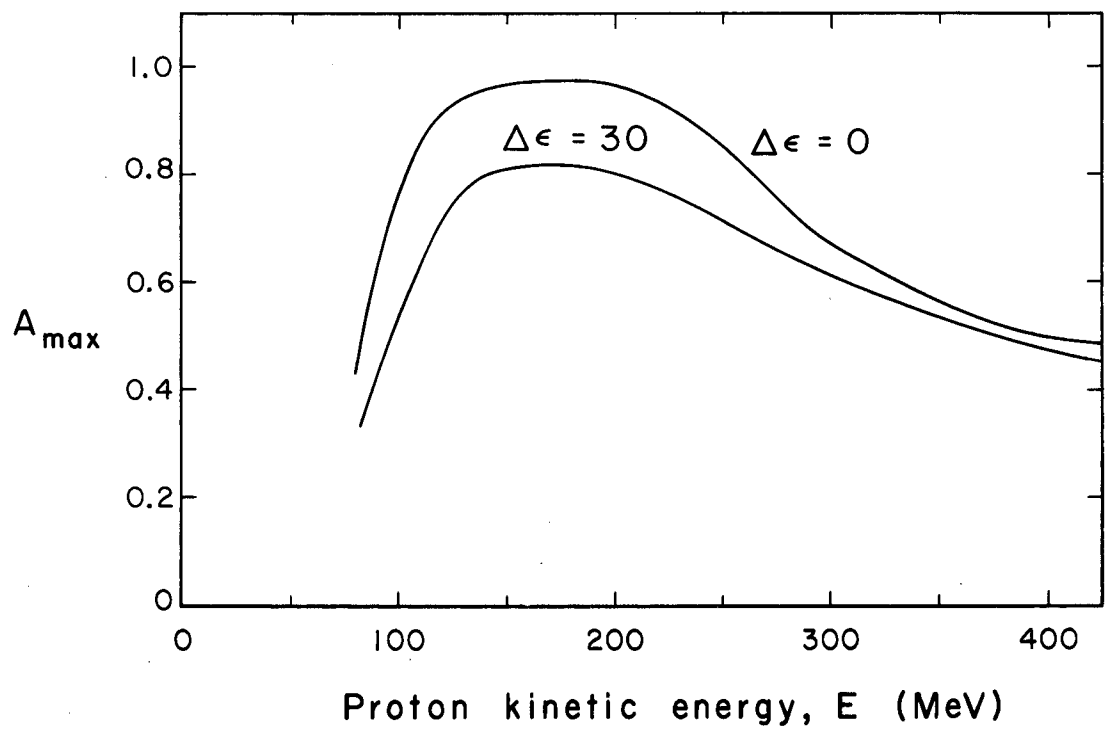
Fig. 13. A_{max} as a function of incident-proton kinetic energy. A_{max} is the largest magnitude the analyzability A ever attains between zero degrees and the diffraction minimum for incoming protons of a given energy.

The likelihood function L(P) was then computed for the sample of events in each specified angular interval of $\cos \theta_\pi^*$; a plot of this function was displayed on the IBM 7090 cathode-ray tube (CRT) and was photographed. By these CRT graphs, any peculiar behavior of the likelihood function, such as a double maxima, could be discovered at a glance and its cause further investigated. A few examples of likelihood functions calculated are given in Fig. 14.

The analyzability was set equal to zero at angles below $\theta(E/180 \text{ MeV})^{1/2} = 4$ deg and above $\theta(E/180 \text{ MeV})^{1/2} = 24$ deg. This ensured that for the proton-energy interval covered, the p-C analyzability does not change sign. Thus a propensity to scattering to the left (looking along particle path) in the chamber always meant a positive (upward) polarization. This is consistent with the convention that the polarization is positive in the direction $(\underset{\sim}{p}_i \times \underset{\sim}{p}_f)$ where $\underset{\sim}{p}_i$ and $\underset{\sim}{p}_f$ are the initial and final pion momenta, respectively.

Finally, the angular intervals (bins) were selected with a width of $\cos \theta_\pi^* = 0.1$ for preliminary analysis, regardless of the size of the event sample this included. This was done in order to explore the general behavior of polarization as a function of $\cos \theta_\pi^*$, such as where and how fast does it change as a function of angle. The angular bins were then shifted a half interval (shift of ± 0.05 in $\cos \theta_\pi^*$) so that we could determine the effect of binning on the polarization values. In all cases the polarization $P(\cos \theta_\pi^*)$ was found to be bin-independent well within the statistical uncertainty of the polarization values. With this knowledge, the final angular bins were chosen as a compromise between enlarging the interval width $\Delta \cos \theta_\pi^*$, to reduce the polarization uncertainty ΔP, and diminishing $\Delta \cos \theta_\pi^*$ so that the loss of structure of $P(\cos \theta_\pi^*)$ would be minimized.
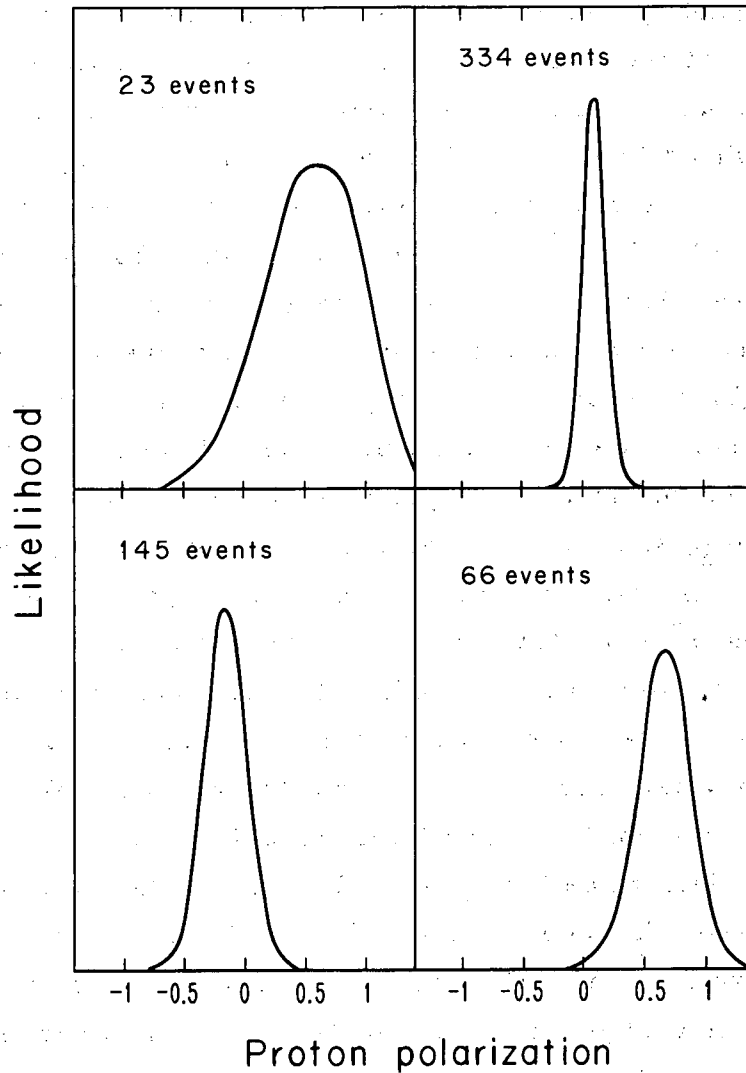
Fig. 14. Examples of likelihood functions L(P) for samples of
polarized protons at four different pion scattering angles
and energies chosen at random.

E. Errors and Corrections

A polarization measurement is performed essentially by determining the number of right scatterings vs the number of left scatterings, and weighting these events according to the effective analyzing power of each. Of the possible systematic errors present those that would effect right and left scatters equally are of less concern than those that effect the right differently from the left. The former affects the statistical uncertainty only, altering the magnitude of the result only slightly. The latter type of error could greatly affect the magnitude and even change the sign of the result. In the following discussion both types of errors are investigated, with particular attention given to the latter type.

1. Scanning Bias and Efficiency

If the scanning method is not completely efficient, so that a certain percentage of the scattering events remain undetected, it is possible that the selection may be biased, in that there may be a greater probability for the detection of a scattering to one side than to the other. If the scanning detection is unbiased, the difference in the scanning efficiency from 100% reduces the confidence in the value of the scattering asymmetry only through the increased statistical uncertainty resulting from the fewer events detected.

Since the scanners conducted their search in a random fashion, bias effects are believed to be small. Most systematic errors in event selection would be expected to be symmetrical, such as measuring the scattering angles too large. The same error would be made on the right scatters as on the left scatters. Any bias must come from a psychological tendency for the scanners to see left-handed rather than right-handed deflections, or the reverse.

The first possible source of bias is the distortions in the scanning projection system and spark-chamber optical system. A systematic asymmetrical error would be introduced by a projection apparatus whose projection optics (lenses, mirrors) were misaligned. In addition, the the only significant optical distortion produced by the spark-chamber optical system was barrel distortion, which was corrected by

installing appropriate corrective lenses in the projection system. By requiring that the illuminated grid superimposed on the proton tracks be orthogonal, the error due to both types of distortion was made small and much less than the average deviation of the angle measurements due to scanner judgment ($\pm$ 1 deg).

Because of this 1-deg uncertainty in angle measurements, scatters greater than 24 deg and less than 5 deg in the lab were arbitrarily eliminated. The fact that no significant up-down asymmetry in the p-C scattering for the accepted protons was found, indicates that any bias introduced by these angle cutoffs is small. Anyway, an asymmetrical error in these cutoff angles between right and left events would have little effect on the final result, because the analyzing power for scatterings near the low cutoff angle is small and only a few events occurred near the large-angle cutoff.

To further investigate these biases, a second scanning was performed on about 75% of the 523-MeV π^- data, 50% of the 689-MeV π^+ data, and 15% of the 572-MeV π^+ data. The 523-MeV π^- and 689-MeV π^+ second scan was performed with the film reversed so that left and right, as viewed by the scanner, was interchanged. I will refer to these scans as "mirror image" scans. A good fraction of the data from these two energies was rescanned in order to investigate (a) bias as a function of event location in the chambers and (b) the reproducibility of the polarization values determined in this experiment. The 572-MeV π^+ film was rescanned in the same manner as first scanned. Every scanner viewed this same film sample so that the possible introduction of personal scanner bias could be detected.

Detection efficiencies (see Appendix D) were measured separately for scattering to the left and to the right, thus providing a measure of the bias, defined as the difference of the right and left efficiencies divided by the sum. Results of the measurements are given in Tables V, VI, and VII.

Table V. Results of 523-MeV π^- double scanning: direct comparison of 15% of the data having scatters with projected angles between 5 and 24 deg.

Events	Left	Right	Sum or average
Found in first scan only	33	24	57
Found in second scan only	39	41	80
Found in both scans	114	117	231
Average efficiency, first scan	75±4%	74±3%	75±2%
Average bias, all scanners, first scan			=1±3%

Table VI. Results of 689-MeV π^+ double scanning: direct comparison of 15% of the data having scatters with projected angles between 5 and 24 deg.

Events	Left	Right	Sum or average
Found in first scan only	95	80	175
Found in second scan only	58	56	114
Found in both scans	177	162	339
Average efficiency, first scan	75±3%	75±3%	75±2%
Average bias, all scanners, first scan			0±3%

Table VII. Results of 572-MeV π^+ double scanning: direct comparison of 15% of the data, individually scanned by each scanner. Only scatters with projected angles between 5 and 24 deg are included.

Scanner	Right efficiency	Left efficiency	Asymmetry
1	72±5%	65±5%	5±5%
2	74±5%	77±5%	-2±5%
3	88±3%	81±3%	4±3%
4	75±4%	77±4%	-1±3%
5	82±3%	85±3%	-2±3%
6	70±4%	69±4%	1±4%
7	86±4%	90±3%	-2±3%

Bias as a function of the location of events in the spark chambers was investigated in two ways.

1. The 523-MeV π^- and 689-MeV π^+ mirror-image scans were processed according to the data-reduction procedure outlined previously, but with the projected angle sense reversed to agree with the first scan. The polarization was then recalculated with these events, by using the same angular bins as before and by making a direct comparison between the mirror image and normal scan. The results of this investigation are given in Tables VIII and IX, where P is the normal-scan polarization, P_m is the mirror-image-scan polarization, and $\overline{\Delta P}$ is the average statistical uncertainty of P and P_m. The quantity $|P_m - P|/\overline{\Delta P}$ was defined as a figure-of-merit parameter to indicate how reproducible and bias-free the polarization is. A value of one or less for this parameter means that the normal and mirror-image polarization agree within the average statistical uncertainty. If the scanning efficiency were 100% and if all the data at these two energies were mirror-image-scanned, the values of the polarization from the two scans should be identical. However, since the scanning efficiency is about 75%, the fact that the parameter $|P_m - P|/\overline{\Delta P}$ differs from zero can be attributed to the fraction (27%) of "new" events detected in each scan.

2. The second method of investigation utilizes the fact that the two chambers overlap so that the polarization of protons recoiling in a particular angular interval can be measured in both chambers. Since the chambers are on opposite sides of the pion beam, the sense of the polarization vector $(\underset{\sim}{p}_i \times \underset{\sim}{p}_f)$ is reversed. Thus, if the polarization in this angular region is due to a propensity to right scatters in one chamber, the other chamber must have a propensity to left scatters (as viewed by the scanner) in order for the polarization to be consistent. Since both chambers afford statistically independent samples, the value of the polarization need only agree within the statistical error. Unfortunately, the only data having enough events in this overlapping region to make significant use of this bias test are 689-MeV π^- and 689-MeV π^+. The results are in Table X.

Table VIII. Comparison of 523-MeV π^- normal and mirror-image scans.

$\cos \theta^*_\pi$	$\Delta \cos \theta^*_\pi$	Normal scan $P \pm \Delta P$	Mirror-image scan $P_m \pm \Delta P_m$	$|P_m - P|/\overline{\Delta P}$
0.250	±0.050	-0.94 ± 0.28	-0.66 ± 0.32	0.94
0.150	±0.050	-0.94 ± 0.22	-0.66 ± 0.22	1.26
0.050	±0.050	-0.34 ± 0.22	-0.24 ± 0.20	0.45
-0.050	±0.050	-0.02 ± 0.24	-0.38 ± 0.22	1.50
-0.150	±0.050	-0.78 ± 0.28	-0.54 ± 0.28	0.86
-0.275	±0.075	0.38 ± 0.22	0.30 ± 0.22	0.36
-0.400	±0.050	0.42 ± 0.26	0.68 ± 0.30	0.93
-0.525	±0.075	0.10 ± 0.16	-0.02 ± 0.18	0.70
-0.675	±0.075	0.10 ± 0.10	0.04 ± 0.12	0.54
-0.825	±0.075	-0.04 ± 0.14	-0.08 ± 0.16	0.27

Table IX. Comparison of 689-MeV π^+ normal and mirror-image scans.

$\cos \theta^*_\pi$	$\Delta \cos \theta^*_\pi$	Normal scan $P \pm \Delta P$	Mirror-image scan $P_m \pm \Delta P_m$	$|P_m - P|/\overline{\Delta P}$
0.375	±0.075	-0.36 ± 0.24	-0.02 ± 0.24	1.41
0.250	±0.050	-0.20 ± 0.22	-0.36 ± 0.20	0.76
0.150	±0.050	-0.32 ± 0.18	-0.18 ± 0.22	0.70
0.025	±0.075	-0.28 ± 0.22	-0.34 ± 0.20	0.28
-0.125	±0.075	0.38 ± 0.32	0.20 ± 0.32	0.56
-0.275	±0.075	0.80 ± 0.20	0.90 ± 0.24	0.45
-0.425	±0.075	0.44 ± 0.20	0.60 ± 0.22	0.76
-0.575	±0.075	0.18 ± 0.16	0.26 ± 0.22	0.42
-0.725	±0.075	0.70 ± 0.16	0.70 ± 0.22	0.00

Table X. Comparison of polarization where chambers A and B overlap.

	$\cos \theta^*_\pi$	P Chamber A	P Chamber B
689 MeV π^-	-0.20 ± 0.10	+0.77 ± 0.25	+0.62 ± 0.32
689 MeV π^+	-0.25 ± 0.10	+0.78 ± 0.28	+0.58 ± 0.38

To summarize, the reproducibility of the polarization values to be quoted in this experiment seem to be consistent with their statistical error. Also, there appears to be little evidence of scanning bias either by the scanning apparatus or by the scanners, taken as a group or individually. If a bias does exist it is small and has little effect in light of the existing large statistical uncertainty of the polarization.

2. Inelastic Scattering

Measurements of the analyzability A as a function of angle and energy loss in scattering show that the analyzability decreases roughly linearly with the energy loss and becomes essentially zero when more than 30 MeV is lost. [25] In order to account for this fact, a correction must be made to the analyzability for the inclusion of inelastic events. A new modified analyzability must be defined, one properly averaged over the analyzabilities of the various unresolvable inelastic states of carbon. If energy losses up to a maximum value of $\Delta\epsilon$ —corresponding to the energy resolution of the detection system— are accepted, the modified analyzability has the form

$$\bar{A}(\theta, E, \Delta\epsilon) = \frac{\int_0^{\Delta\epsilon} A(\theta, E, \epsilon)\, \frac{d^2\sigma}{d\Omega\, d\epsilon}\, d\epsilon}{\int_0^{\Delta\epsilon} \frac{d^2\sigma}{d\Omega\, d\epsilon}\, d\epsilon} \quad ,$$

where ϵ is the energy loss, and $\frac{d^2\sigma}{d\Omega\, d\epsilon}(\theta, E)$ is the double differential cross section for inelastically scattered protons from carbon.

In our case the maximum energy loss accepted, $\Delta\epsilon$, was taken to be 30 MeV. This energy cutoff was determined by investigating the energy distribution of the accepted events about the theoretically calculated recoil-proton energy, T_k. These energy distributions are given in Fig. 15(a), (b), (c) for the three beam energies. The events used were produced by incident π^-'s but very similar distributions are obtained from π^+ data, as would be expected since this should be a purely kinematic result. These energy distributions have a characteristic half-width of about 30 MeV and are asymmetrical, with more events on
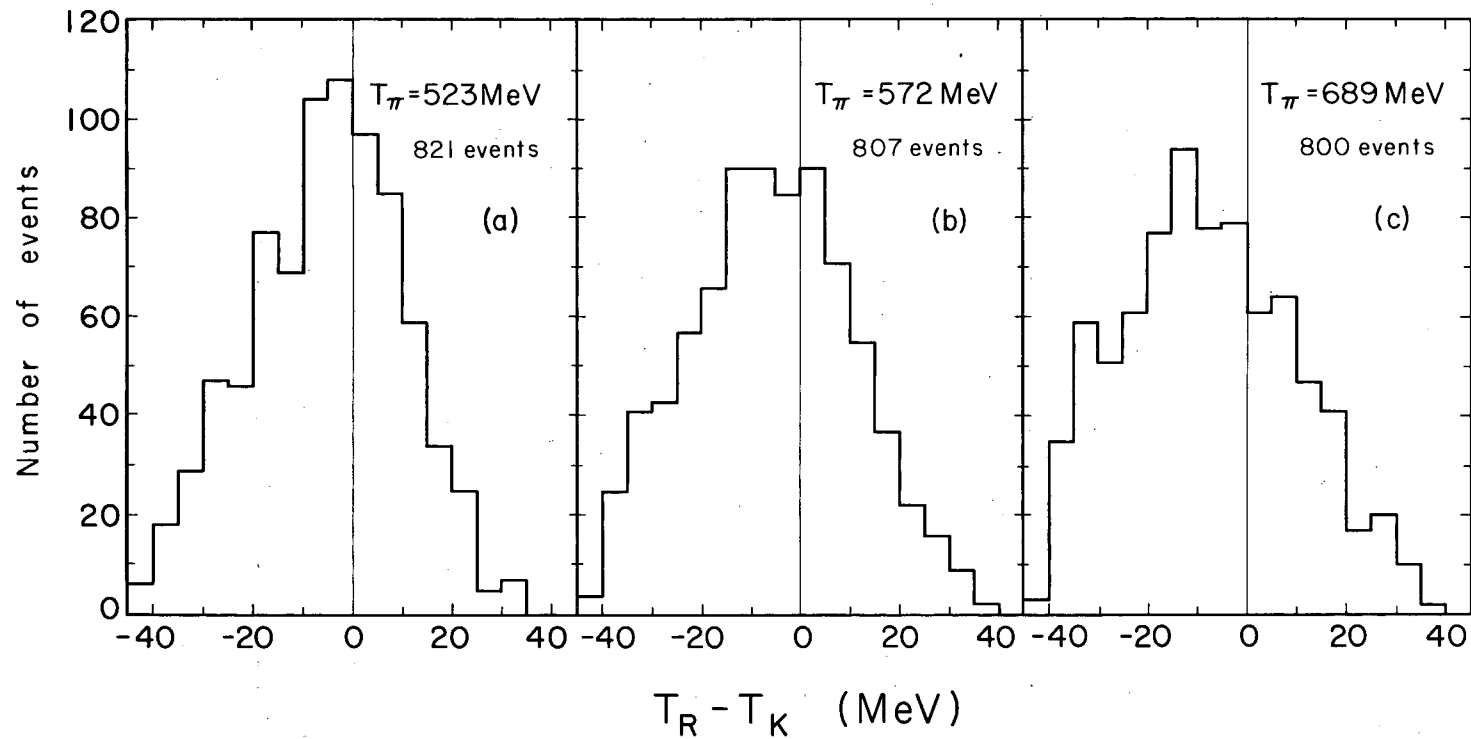
Fig. 15. Energy distributions of accepted events about the kinematically calculated recoil-proton energy T_K; T_R is the recoil proton energy determined by range in carbon.

MUB-1664

the low side, consistent with energy loss in p-C scattering. The major contribution to the width is due to the ± 3% momentum band of the incident pions.

Peterson[25] gives, and Fig. 12 reproduces, a modified analyzability—which includes inelastic scatters with energy losses of up to 30 MeV—as a function of proton energy and angle. The magnitude of the correction for inelastics included in a given sample of events depends on the angular distribution of the sample. But, on the average, since the accepted events possess scattering angles in the angular region where it is believed that the inelastic scattering is a few percent of the elastic, the correction is quite small. In general, the magnitude of the corrected polarization is increased since the modified analyzability is smaller than the analyzability for elastics only. For comparison purposes, Sec. IV gives the polarization calculated by using the weighted average $A(\theta, E, \Delta\epsilon)$, with $\Delta\epsilon = 0$, and also with $\Delta\epsilon = 30$ MeV.

3. Analyzing-Power Uncertainty

The uncertainty in the polarization resulting from the uncertainty in the analyzing power can be obtained by investigating the changes in the calculated polarization when the analyzability is modified within the limits of the error $A(E, \theta)$ obtained from p-C scattering experiments. Thus the parameter $A(E, \theta)$ was altered ± 0.05, corresponding to the average empirical uncertainty of the p-C scattering experiments, and the polarization recalculated. The deviation from quoted values of course depended on the make-up of the sample. Average deviation in polarization was 0.03. This test of the sensitivity of the data due to a systematically high or low analyzability gives an upper limit of the possible deviation in polarization, since it is highly unlikely that the p-C scattering measurements are either all high or all low.

IV. EXPERIMENTAL RESULTS

A. Data

Tables XI to XVI give the polarization $P(\cos\theta_\pi^*)$ determined in this experiment for elastic $\pi^\pm p$ scattering at 523, 572, and 689 MeV. These quoted values do not include the error in polarization resulting from uncertainty in analyzing power (Sec. III. E. 3) and bias measurements (Sec. III. E. 1). Only the statistical uncertainty is shown, the other uncertainties being negligible in comparison.

B. Curve Fitting

An analysis, which used the phase shift formalism (Appendix B) in an attempt to get a best fit to all the available data at the above energies, was performed by using the following experimental data:

1. Polarization data of this experiment,
2. Total cross section,[3,4]
3. Differential cross sections,[10]
4. Real part of the forward scattering amplitude.[26]

The curves thus determined, computed by using plausible but nonunique sets of phase shifts, are shown in Figs. 16 to 21, along with the data points. The solid-line curves are those computed from a phase shift set consistent with a D_{13} resonance, while the dashed-line curves are computed by using a phase shift set consistent with P_{13} resonance at 600 MeV. If a dashed-line curve is not shown it means that for all practical purposes the two curves are the same. For a detailed discussion on how these phase shift sets were determined, and their significance, the reader is referred to Sec. V.

Table XI. Recoil-proton polarization for $\pi^- + p \to \pi^- + p$ as a function of the cosine of c. m. pion scattering angle at 523-MeV incident-pion kinetic energy.

$\cos \theta_\pi^*$	$\cos \theta_\pi^*$	Polarization	
		With inelastic correction	Without inelastic correction
+0.250±0.050	0.249	-0.94±0.26	-0.78±0.24
+0.150±0.050	0.155	-0.94±0.20	-0.82±0.18
+0.050±0.050	0.054	-0.34±0.20	-0.30±0.18
-0.050±0.050	-0.045	-0.02±0.24	-0.04±0.20
-0.150±0.050	-0.146	-0.78±0.28	-0.70±0.24
-0.275±0.075	-0.273	+0.38±0.20	+0.32±0.18
-0.400±0.050	-0.409	+0.42±0.26	+0.42±0.22
-0.525±0.075	-0.533	+0.10±0.16	+0.04±0.14
-0.675±0.075	-0.678	+0.10±0.10	+0.10±0.09
-0.825±0.075	-0.790	-0.04±0.14	-0.04±0.12

Table XII. Recoil proton polarization for $\pi^+ + p \to \pi^+ + p$ as a function of the cosine of c. m. pion scattering angle at 523-MeV incident-pion kinetic energy.

$\cos \theta_\pi^*$	$\cos \theta_\pi^*$	Polarization	
		With inelastic correction	Without inelastic correction
+0.250±0.050	+0.243	-0.26±0.32	-0.24±0.26
+0.150±0.050	+0.155	-0.34±0.19	-0.28±0.16
+0.050±0.050	+0.054	-0.42±0.17	-0.38±0.16
-0.050±0.050	-0.045	-0.44±0.20	-0.42±0.18
-0.175±0.075	-0.167	+0.20±0.28	+0.18±0.24
-0.325±0.075	-0.326	-0.56±0.30	-0.50±0.26
-0.475±0.075	-0.508	-0.10±0.34	-0.10±0.29
-0.625±0.075	-0.638	-0.36±0.17	-0.34±0.15
-0.775±0.075	-0.758	-0.14±0.21	-0.14±0.19

Table XIII. Recoil-proton polarization for $\pi^- + p \to \pi^- + p$ as a
function of the cosine of c.m. pion scattering angle at 572-MeV
incident-pion kinetic energy.

$\cos\theta^*_\pi$	$\cos\theta^*_\pi$	Polarization	
		With inelastic correction	Without inelastic correction
+0.300±0.050	+0.300	-0.56±0.36	-0.48±0.30
+0.200±0.050	+0.205	-0.26±0.24	-0.20±0.21
+0.100±0.050	+0.110	-0.58±0.19	-0.50±0.18
-0.025±0.075	-0.013	-0.36±0.20	-0.34±0.18
-0.175±0.075	-0.176	-0.18±0.29	-0.16±0.25
-0.300±0.050	-0.305	+0.64±0.39	+0.54±0.35
-0.400±0.050	-0.409	+0.12±0.33	+0.08±0.28
-0.500±0.050	-0.513	-0.10±0.23	-0.06±0.20
-0.600±0.050	-0.610	-0.62±0.15	-0.50±0.14
-0.700±0.050	-0.708	-0.58±0.14	-0.52±0.12
-0.800±0.050	-0.791	-0.38±0.19	-0.30±0.16

Table XIV. Recoil proton polarization for $\pi^+ + p \to \pi^+ + p$ as a
function of the cosine of c.m. pion scattering angle at 572-MeV
incident-pion kinetic energy.

$\cos\theta^*_\pi$	$\cos\theta^*_\pi$	Polarization	
		With inelastic correction	Without inelastic correction
+0.300±0.050	+0.290	+0.14±0.26	+0.08±0.22
+0.200±0.050	+0.195	-0.12±0.16	-0.12±0.14
+0.100±0.050	+0.104	-0.22±0.16	-0.16±0.14
0.000±0.050	+0.003	-0.30±0.16	-0.24±0.14
-0.100±0.050	-0.099	-0.12±0.24	-0.08±0.22
-0.225±0.075	-0.229	+0.38±0.22	+0.30±0.20
-0.375±0.075	-0.370	+0.64±0.28	+0.60±0.24
-0.525±0.075	-0.542	+0.44±0.24	+0.36±0.22
-0.650±0.060	-0.650	+0.22±0.20	+0.18±0.18
-0.775±0.075	-0.758	-0.14±0.20	-0.16±0.18

Table XV. Recoil proton polarization for $\pi^- + p \rightarrow \pi^- + p$ as a function of the cosine of c. m. pion scattering angle at 689-MeV incident-pion kinetic energy.
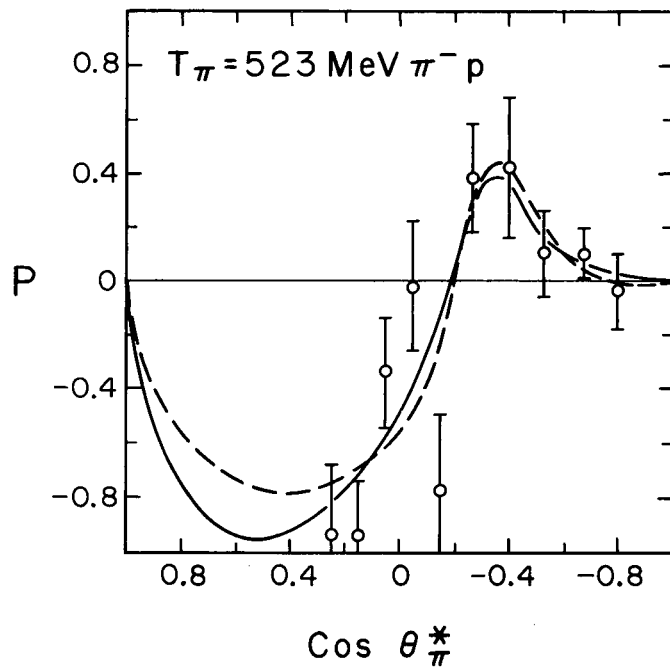
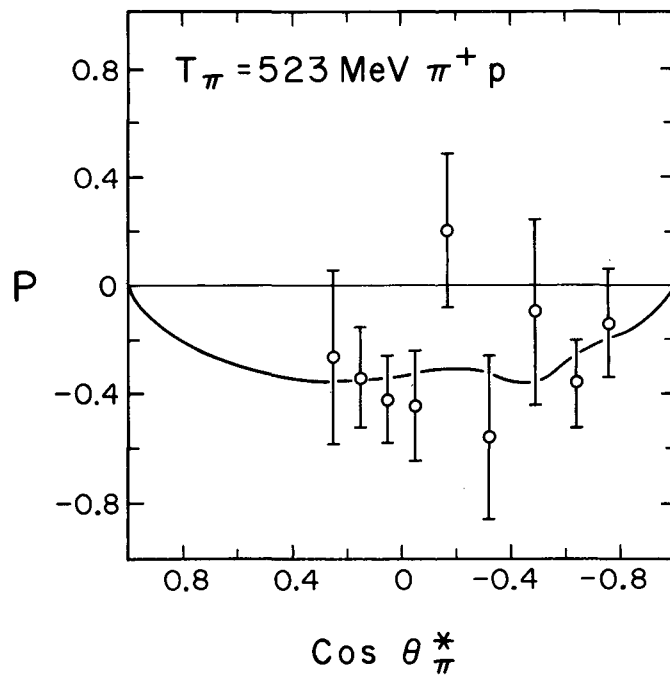| $\cos \theta^*_\pi$	$\cos \theta^*_\pi$	Polarization	
		With inelastic correction	Without inelastic correction
+0.350±0.050	+0.341	-0.48±0.34	-0.46±0.32
+0.250±0.050	+0.249	-0.28±0.24	-0.26±0.20
+0.150±0.050	+0.156	-0.20±0.22	-0.18±0.20
+0.050±0.050	+0.054	-0.14±0.22	-0.08±0.20
-0.050±0.050	-0.040	+0.54±0.30	+0.48±0.26
-0.175±0.075	-0.192	+0.70±0.20	+0.58±0.18
-0.325±0.075	-0.333	+0.06±0.18	+0.02±0.18
-0.450±0.050	-0.456	+0.02±0.22	+0.04±0.20
-0.550±0.050	-0.551	-0.16±0.16	-0.14±0.15
-0.650±0.050	-0.654	-0.44±0.16	-0.42±0.15
-0.750±0.050	-0.750	-0.24±0.18	-0.18±0.17

Table XVI. Recoil-proton polarization for $\pi^+ + p \rightarrow \pi^+ + p$ as a function of the cosine of c. m. pion scattering angle at 689 MeV incident-pion kinetic energy.

$\cos \theta^*_\pi$	$\cos \theta^*_\pi$	Polarization	
		With inelastic correction	Without inelastic correction
+0.375±0.075	+0.364	-0.36±0.24	-0.32±0.20
+0.250±0.050	+0.251	-0.20±0.22	-0.16±0.18
+0.150±0.050	+0.159	-0.32±0.20	-0.28±0.17
+0.025±0.075	+0.026	-0.28±0.22	-0.22±0.20
-0.125±0.075	-0.111	+0.38±0.32	+0.32±0.30
-0.275±0.075	-0.277	+0.80±0.22	+0.68±0.19
-0.425±0.075	-0.435	+0.44±0.20	+0.46±0.18
-0.575±0.075	-0.573	+0.18±0.17	+0.14±0.15
-0.725±0.075	-0.705	+0.70±0.18	+0.64±0.17

Fig. 16. Recoil-proton polarization for $\pi^- + p \rightarrow \pi^- + p$ as a function of the cosine of c.m. pion scattering angle at an incident-pion kinetic energy of 523 MeV. The solid line is a polarization curve computed from a phase shift set, assuming a D_{13} resonance. The dashed line is computed by using an assumed P_{13} resonance phase shift set.

Fig. 17. Recoil-proton polarization for $\pi^+ + p \to \pi^+ + p$ as a function of the cosine of c. m. pion scattering angle at an incident-pion kinetic energy of 523 MeV.
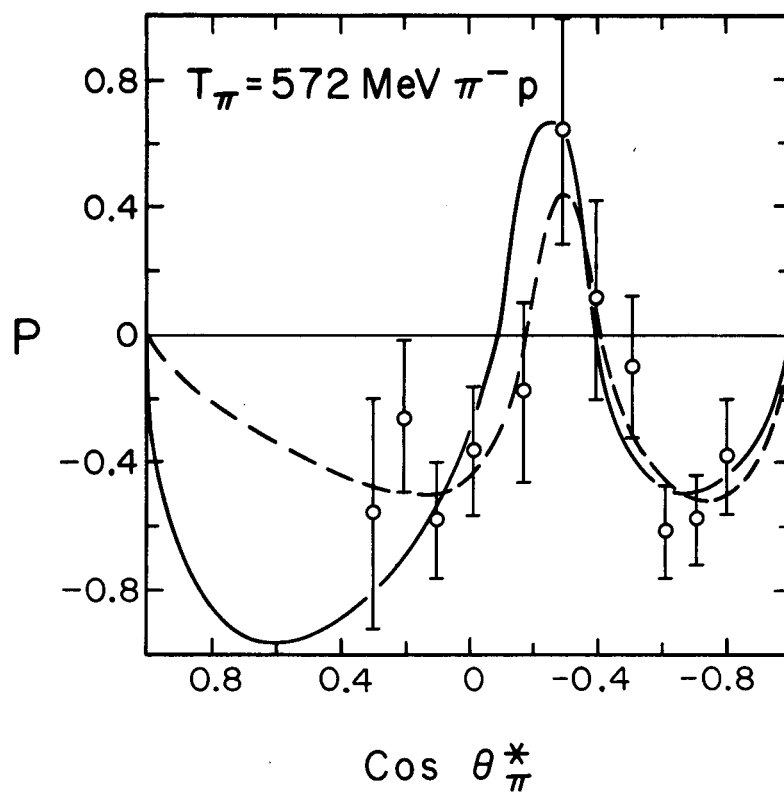
MU-29841

Fig. 18. Recoil-proton polarization for $\pi^- + p \rightarrow \pi^- + p$ as a
function of the cosine of c. m. pion scattering angle at an
incident-pion kinetic energy of 572 MeV. The solid line is
a polarization curve computed from a phase shift set,
assuming a D_{13} resonance. The dashed line is computed
by using an assumed P_{13} resonance phase shift set.

Fig. 19. Recoil-proton polarization for $\pi^+ + p \rightarrow \pi^+ + p$ as a function of the cosine of c. m. pion scattering angle at an incident-pion kinetic energy of 572 MeV.
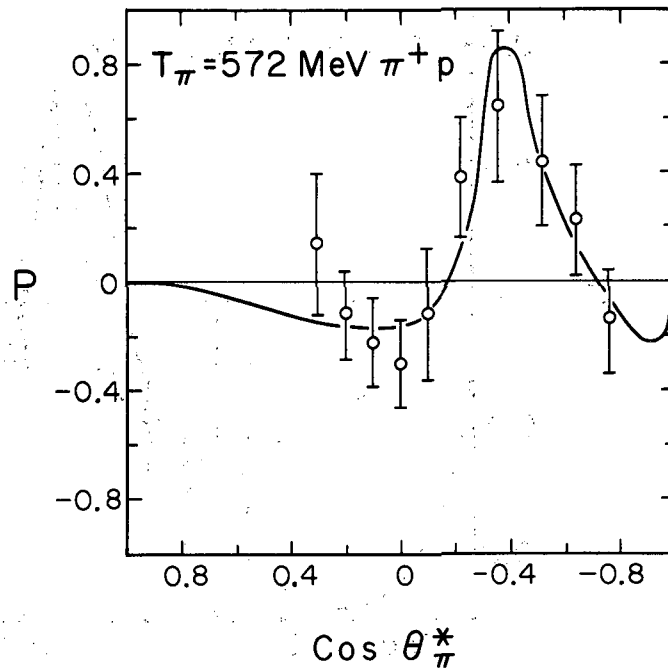
Fig. 20. Recoil-proton polarization for $\pi^- + p \rightarrow \pi^- + p$ as a function of the cosine of c. m. pion scattering angle at an incident-pion kinetic energy of 689 MeV. The solid line is a polarization curve computed from a phase shift set, assuming a D_{13} resonance. The dashed line is computed by using an assumed P_{13} resonance phase shift set.
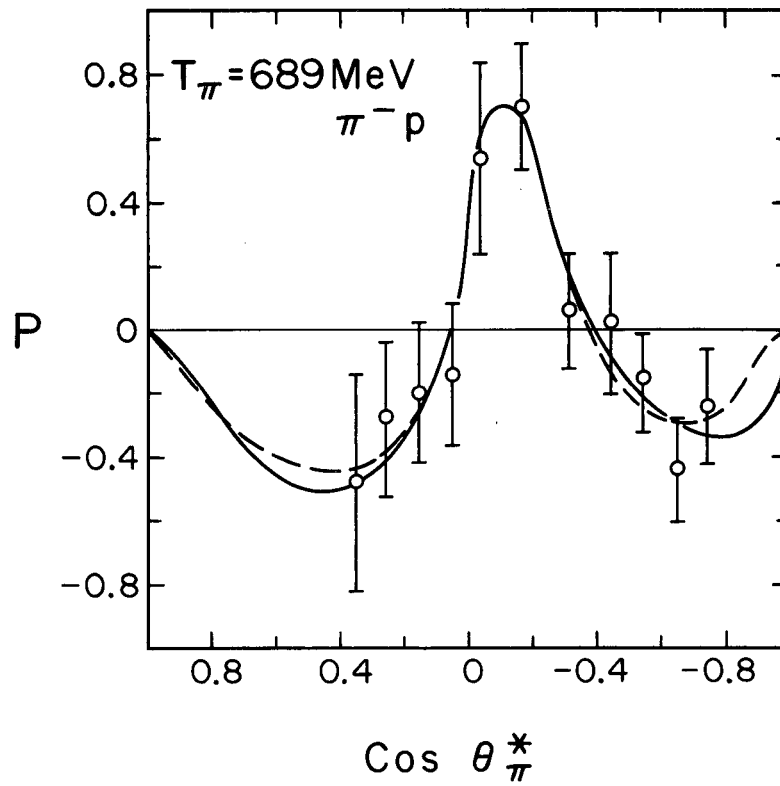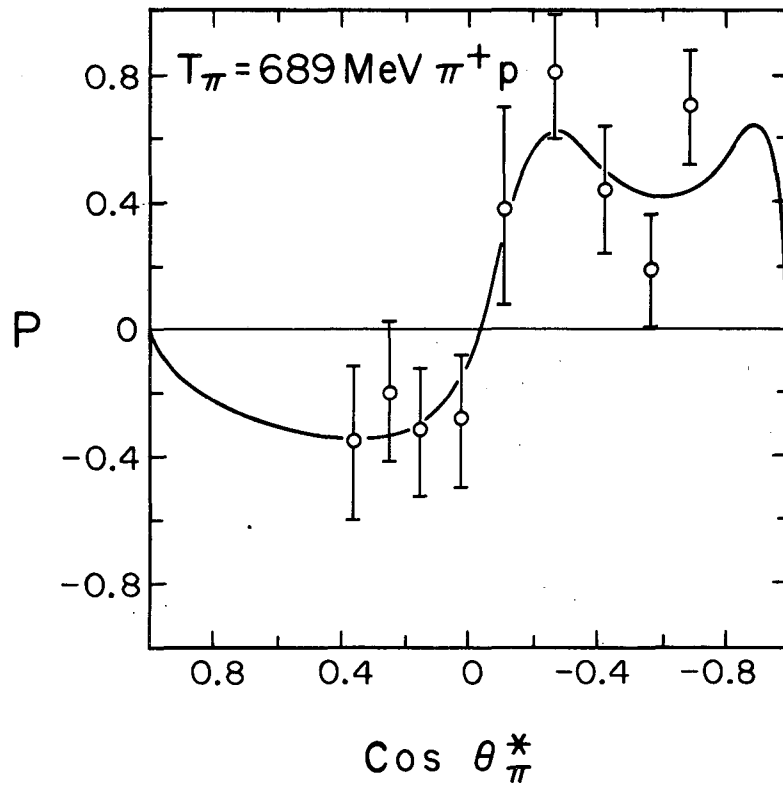
Fig. 21. Recoil-proton polarization for $\pi^+ + p \to \pi^+ + p$ as a
function of the cosine of c.m. pion scattering angle at an
incident-pion kinetic energy of 689 MeV.

V. DISCUSSION

It is well known[16] that the product of the polarization and the differential cross section at a given energy can be written as a power series in $\cos \theta_\pi^*$:

$$\frac{P(\theta_\pi^*) \, \sigma(\theta_\pi^*)}{\sin \theta_\pi^*} = \sum^{2(\ell_{max})-1}_n b_n \cos^n \theta_\pi^* \quad ,$$

where the b's are linear combinations of products between partial-wave amplitudes (see Appendix B), and ℓ_{max} is the state of maximum angular momentum involved in the scattering. Hence, if we fit out data to an expansion of this form we should obtain information on what particular states are contributing to the interaction.

A least-squares fit was made of this cosine power series to the polarization data. The series was terminated by applying standard statistical tests[27] in conjunction with whatever characteristics of the πN interaction are indicated by scattering experiments.[10] The results are given in Tables XVII and XVIII. From these tables we can see immediately that the statistical accuracy of the data of this experiment is unable in itself to resolve the presence or absence of the higher angular momentum states which manifest themselves in the coefficients of higher powers of $\cos \theta_\pi^*$. The lower power coefficients, b_0 and b_1, are reliably determined, in that they did not deviate in magnitude or sign as we increased the order of fit. However, b_3 and b_4 tended to deviate significantly, depending on what order of fit was chosen. This was reflected in the violent fluctuations of the polarization with order of fit in the angular region of no data. It is also reflected in the large errors of the higher power coefficients.

If we accept the results of Table XVII, then the fact that no particular coefficients stand out to dominate the expansion indicates that the number of states that are excited to a greater or lesser degree must be large. If there is one angular momentum state which really dominates in this energy region, its signature is hidden by its inter-ference with the numerous other states present. This is also confirmed

Table XVII. Coefficients b_n from the expansion $\dfrac{P(\theta)\sigma(\theta)}{\sin\theta} = \sum\limits_{n=0}^{n} b_n \cos^n\theta$, obtained by fitting polarization data only.

Incident-pion energy (MeV)	b_0 (mb)	b_1 (mb)	b_2 (mb)	b_3 (mb)	b_4 (mb)
$\pi^+ p$					
523	-0.143 ± 0.039	-0.802 ± 0.290	-1.570 ± 0.0928	-0.909 ± 0.861	-
572	-0.0517 ± 0.027	-0.307 ± 0.189	-0.058 ± 0.656	0.381 ± 0.655	-
689	0.003 ± 0.027	-0.427 ± 0.117	-0.940 ± 0.555	-1.021 ± 0.748	-
$\pi^- p$					
523	-0.217 ± 0.062	-1.674 ± 0.347	-3.115 ± 1.388	-1.795 ± 1.537	-
572	-0.179 ± 0.043	-1.211 ± 0.313	-0.809 ± 1.278	2.397 ± 1.479	-
689	0.055 ± 0.041	-0.910 ± 0.308	-2.405 ± 1.116	1.989 ± 4.409	3.284 ± 4.967

Table XVIII. Values of χ^2 and $(\chi^2/D)^{1/2}$, and number of data points used for the order fit chosen.

Incident-pion energy (MeV)	No. of data points	Order of Fit, N	Degrees of freedom, D	χ^2	$(\chi^2/D)^{1/2}$
$\pi^+ p$					
523	9	3	5	6.00	1.10
572	10	3	6	3.91	0.81
689	9	3	5	7.41	1.22
$\pi^- p$					
523	12	3	8	9.79	1.10
572	11	3	7	4.83	0.83
689	11	4	6	2.66	0.67

by angular-distribution and photo-production experiments.[6,7] Therefore, the assumption that the πN interaction at these energies is dominated by the influence of neighboring single-state resonances as proposed by Moravcsik[16] is unfortunately oversimplified.

In order to circumvent the above problem, an attempt was made to utilize all the available data on πN scattering at these three energies, in the hopes of constraining the polarization in the angular region of no data to agree with this independent data. The conventional formalism for doing this is phase shift analysis, which essentially amounts to a simultaneous least-squares fit of all the available data in terms of a given number of partial-wave amplitudes. Scattering experiments[10] indicate that no angular momentum states higher than $\ell = 3$ contribute significantly at energies below 1 BeV. Thus an attempt was made to use total and differential cross sections and the real part of forward scattering amplitude, $D(0)$, as well as polarization, in order to obtain a best fit to Eqs. (B-4), (B-5), and (B-6) of Appendix B, by using up to and including F waves. This was accomplished by using a computer to search for sets of amplitudes that agree with existing data. A tentative set of phase shifts is fed into the computer program and the computer then varies the phase shifts in such a way as to minimize the quantity

$$\chi^2 = \sum \left\{ \left| \frac{\frac{d\sigma^c}{d\Omega} - \frac{d\sigma^{exp}}{d\Omega}}{\Delta \frac{d\sigma}{d\Omega}} \right|^2 + \left| \frac{\sigma_T^c - \sigma_T^{exp}}{\sigma_T} \right|^2 + \left| \frac{D^c(0) - D^{exp}(0)}{\Delta D(0)} \right|^2 + \left| \frac{P^c - P^{exp}}{\Delta P} \right|^2 \right\}$$

where the superscripts c and exp indicate the calculated and experimental values of the data point, respectively, and Δ indicates the corresponding uncertainty directly or indirectly from experiment. The summation is over all experimental quantities being considered for both pion charge states.

By this method many sets of phase shifts were obtained for each of the three energies by feeding random sets of phase shifts as input to the computer, then allowing the computer to converge on a best fit.

A good number of these solutions gave qualitatively different sets of
phase shifts, making the attainment of a unique solution to the problem
impossible.

Since existing data[2-4] favor a resonance having the quantum
numbers $J = 3/2$, $T = 1/2$, and either even or odd parity at 600 MeV,
a less ambitious attempt was made to find a set of phase shifts at 523,
572, and 689 MeV that would satisfy one of the following sets of restric-
tive assumptions:

1. a. A D-wave, iso-spin 1/2, angular momentum 3/2, highly
absorptive resonance exists at 600 MeV; the other nonresonant states
behave "normally."

b. A P-wave, iso-spin 1/2, angular momentum 3/2, highly
absorptive resonance exists at 600 MeV; the other nonresonant states
behave "normally."

2. The phase shift sets at the three energies must be consistent
among themselves and agree with the lower-energy phase shifts.[28] This
demands that the value of the phase shift for each state must vary
smoothly with energy, as expected from causality.

3. The value of χ^2 must indicate a good fit to the data.[27] I
shall refer to the set of assumptions 1a, 2, and 3 as "the D_{13} case"
and the assumptions 1b, 2, and 3 as "the P_{13} case."

The two states (1a and 1b) have the same angular distribution
and total cross section since they possess the same J value (Minami
ambiguity). Thus with the inclusion of the polarization data of this ex-
periment, we hoped to satisfy either one set of assumptions or the
other, and thereby resolve the parity of the resonant state. It must be
remembered that phase shifts that satisfy one of the above sets of re-
strictions would be only a plausible, nonunique solution to the problem.
Nevertheless, it would establish that all the available $\pi^{\pm} p$ data are con-
sistent with either a P_{13} resonant state as predicted by Wilson,[29] or
a D_{13} resonant state as predicted by Peierls.[8] Recent measure-
ments[13-15] of the polarization of recoil protons in photoproduction

have been interpreted as favoring the D_{13} case; however, it has since been pointed out by Landovitz and Marshall[30] that all the results of photoproduction, including the polarization, can be explained by an interference between a P_{13} resonance at 600 MeV and a third resonance of proper parity.

With this in mind, we fed sets of phase shifts favoring the D_{13} case to the computer as input information. The computer was then permitted to vary all the phase shifts and obtain solutions at each energy which one hoped would preserve the qualitative behavior of the original input set. The same procedure was followed for the P_{13} case. A consistent and plausible set of phase shifts was found at each energy for both cases; these are given in Tables XIX A and XIX B.

Table XX gives the pertinent information concerning best-fit criteria. The χ^2 at 572 MeV seems to be considerably higher than the expected χ^2 for both cases. This condition seems to be inherent in the experimental data, as can be judged from the fact that no χ^2 value better than 55 has ever been attained from the countless solutions obtained from feeding sets of random phase shifts as input information to the program. These particular sets of phase shifts, from a statistical point of view, possess the typical behavior of the numerous other sets found.

Values of the coefficients of the cosine power series for polarization and differential cross sections as calculated from these phase shifts are tabulated in Tables XXI A and XXI B. The polarization coefficients for both cases are essentially the same as the b's obtained by fitting just the polarization data (Table XVII). Any differences may be explained by the additional constraints imposed on the behavior of the polarization in the angular region of no data by the total and differential cross sections and the real part of the forward scattering amplitude. The differential-cross-section coefficients are in essential agreement with Helland et al.,[31] whose coefficients were obtained by fitting only angular distribution data.

Table XIX A. A plausible but nonunique set of phase shifts, consistent with a D_{13} resonance, obtained by fitting $\pi^{\pm}p$ total and differential cross sections, real part of forward scattering amplitude, and polarization.

State	523 MeV		572 MeV		689 MeV	
$\ell_{2T, 2J}$	δ(deg)	η	δ(deg)	η	δ(deg)	η
$S_{3,1}$	-22.6	0.82	-22.3	1.00	-16.6	1.00
$P_{3,1}$	- 1.9	0.83	- 6.7	0.79	- 9.1	0.65
$P_{3,3}$	155.2	1.00	159.3	1.00	159.7	0.97
$D_{3,3}$	4.6	0.98	2.8	0.98	- 4.0	0.85
$D_{3,5}$	- 9.4	0.94	- 8.0	0.89	0.8	0.93
$F_{3,5}$	- 1.0	1.00	0.6	1.00	2.5	0.95
$F_{3,7}$	0.6	1.00	3.5	0.98	1.8	0.96
$S_{1,1}$	- 2.4	0.25	-37.6	0.49	-42.4	0.71
$P_{1,1}$	6.1	0.52	21.6	0.71	16.7	0.54
$P_{1,3}$	0.6	1.00	- 3.0	1.00	-14.5	0.60
$D_{1,3}$	43.4	0.84	61.7	0.47	151.9	0.40
$D_{1,5}$	4.8	0.93	1.6	0.91	10.7	0.88
$F_{1,5}$	6.0	1.00	17.3	1.00	13.2	0.93
$F_{1,7}$	0.8	0.99	- 0.8	0.97	3.9	0.99

Table XIX B. A plausible but nonunique set of phase shifts, consistent with a P_{13} resonance, obtained by fitting $\pi^{\pm}p$ total and differential cross sections, real part of forward scattering amplitude, and polarization.

State	523 MeV		572 MeV		689 MeV	
$\ell_{2T, 2J}$	δ(deg)	η	δ(deg)	η	δ(deg)	η
$S_{3, 1}$	-21.8	0.81	-22.5	0.97	-16.9	1.00
$P_{3, 1}$	- 1.0	0.84	- 7.0	0.80	- 6.5	0.64
$P_{3, 3}$	155.2	0.99	158.4	0.98	159.2	0.94
$D_{3, 3}$	4.9	0.99	2.5	1.00	- 3.6	0.86
$D_{3, 5}$	- 9.9	0.94	- 7.4	0.89	0.1	0.94
$F_{3, 5}$	- 1.0	1.00	- 0.8	1.00	2.9	0.97
$F_{3, 7}$	0.4	1.00	3.1	1.00	1.5	0.96
$S_{1, 1}$	32.6	0.05	7.5	0.18	-10.4	0.49
$P_{1, 1}$	18.7	1.00	37.8	0.42	- 2.0	0.28
$P_{1, 3}$	40.2	0.65	81.3	0.38	133.8	0.58
$D_{1, 3}$	10.4	0.96	7.7	1.00	9.2	0.53
$D_{1, 5}$	- 6.3	0.96	1.5	0.96	5.4	0.95
$F_{1, 5}$	1.5	1.00	2.6	1.00	6.0	1.00
$F_{1, 7}$	6.6	1.00	5.9	1.00	7.4	0.91

Table XX. Values of χ^2 found for solutions in Tables XIX A and XIX B.

	523 MeV	572 MeV	689 MeV
Number of data points fitted, N [a]	53	57	58
Number of parameters varied [b]	28	28	28
χ^2, assuming D_{13} resonance	37	62	27
χ^2, assuming P_{13} resonance	38	54	27
Best χ^2 value ever attained, assuming no resonance [c]	37	55	27
χ^2 expected [d]	25	29	30

[a] Experimental data used, besides polarization, was taken from references 3, 4, 10, and 26.

[b] If we include up to $\ell = 3$, we have two spin orientations for each angular momentum state except $\ell = 0$, the real and imaginary parts of the phase shifts for each partial wave, and two possibilities for the value of the isotopic spin of each wave, giving a total of 28 independent parameters.

[c] This value is the best value of χ^2 obtained by looking at countless phase shift sets obtained by random-search procedure.

[d] Here χ^2_{exp} means the number of degrees of freedom; that is, the number of experimental points fitted minus the number of phase shifts varied.

Table XXI A. Values of the coefficients a_n and b_n from the expansions

$$\sigma(\theta) = \lambda^2 \sum_n a_n \cos^n\theta \quad \text{and} \quad \frac{P(\theta)\sigma(\theta)}{\sin\theta} = \lambda^2 \sum_n b_n \cos^n\theta$$

calculated from the phase shifts in Table XIX A.

Coefficients[a]	523 MeV		572 MeV		689 MeV	
	$\pi^+ p$	$\pi^- p$	$\pi^+ p$	$\pi^- p$	$\pi^+ p$	$\pi^- p$
a_0	0.21	0.18	0.18	0.17	0.11	0.14
a_1	0.97	0.67	0.94	0.92	0.54	0.60
a_2	1.33	1.02	1.48	1.78	1.58	2.55
a_3	-0.05	-0.06	-0.24	0.14	-0.16	-0.73
a_4	-0.44	0.33	-1.13	0.13	-1.83	-2.28
a_5	0.15	0.05	0.10	0.23	0.26	1.94
a_6	-0.00	0.00	0.30	0.08	0.86	1.75
b_0	-0.06	-0.09	-0.03	-0.06	-0.01	0.04
b_1	-0.30	-0.68	-0.17	-0.81	-0.30	-0.52
b_2	-0.48	-1.16	-0.04	-1.84	-0.38	-1.59
b_3	-0.16	-0.88	0.22	-1.28	-0.05	0.07
b_4	0.07	-0.36	0.03	-1.55	0.31	0.98
b_5	0.00	-0.04	-0.01	-0.62	0.01	0.34

[a]To compare these coefficients with Table XVII the coefficients must be multiplied by λ^2. Here λ^2 = 2.21, 1.99, and 1.60 mb for T_π = 523, 572, and 689 MeV, respectively.

Table XXI B. Values of coefficients a_n and b_n from the expansions

$$\sigma(\theta) = \lambda^2 \sum_n a_n \cos^n\theta \quad \text{and} \quad \frac{P(\theta)\sigma(\theta)}{\sin\theta} = \lambda^2 \sum_n \cos^n\theta$$

calculated from the phase shifts in Table XIX B.

Coefficients[a]	523 MeV		572 MeV		689 MeV	
	$\pi^+ p$	$\pi^- p$	$\pi^+ p$	$\pi^- p$	$\pi^+ p$	$\pi^- p$
a_0	0.20	0.19	0.18	0.18	0.10	0.14
a_1	0.97	0.78	0.93	1.06	0.53	0.61
a_2	1.33	1.08	1.43	1.96	1.57	2.51
a_3	-0.04	-0.64	-0.20	-0.38	-0.11	-0.69
a_4	-0.43	0.05	-0.96	-0.35	-1.79	-2.33
a_5	0.14	0.58	0.10	0.57	0.21	1.84
a_6	-0.00	0.15	0.18	0.46	0.82	1.87
b_0	-0.06	-0.12	-0.03	-0.09	-0.01	0.03
b_1	-0.30	-0.77	-0.16	-0.69	-0.30	-0.55
b_2	-0.51	-0.92	-0.03	-0.77	-0.35	-1.52
b_3	-0.21	-0.06	0.21	0.76	0.03	0.77
b_4	0.04	0.15	0.04	-0.01	0.21	1.13
b_5	0.00	0.03	0.00	0.00	-0.19	-0.67

[a]To compare these coefficients with Table XVII the coefficients must by multiplied by λ^2; $\lambda^2 = 2.21$, 1.99, and 1.60 mb for $T_\pi = 523$, 572, and 689 MeV, respectively.

Qualitatively, the phase shift sets for both cases have a reasonable behavior with respect to incident-pion energy. The strong S- and P-wave absorption in the T = 1/2 channel is consistent with the behavior of the cross section for pion production observed at these and lower energies.[32] The only significant departure from the "normal" behavior is in the phase shift for the J = 3/2, T = 1/2 P- or D-wave state, which possesses an assumed resonant behavior at 600 MeV. That both cases agree with the abundant $\pi^{\pm}$p data available is an indication of the accuracy of the polarization data needed to resolve the parity of a given state. Although the D_{13} case is favored by the various πN and $\pi\pi$ isobar models proposed by Peierls[33] and Ball and Frazer[34] to explain the higher-energy maxima, the statistical accuracy of the polarization data measured in this experiment cannot resolve the two cases. This is most strikingly seen in Figs. 16 to 21, where the computed curves for both cases are presented. Clearly, more experimental information, such as charge exchange angular distributions or recoil-proton polarization data with far smaller statistical uncertainty, is needed to ultimately obtain a unique set of angular momentum amplitudes (phase shifts) that will completely determine πN scattering at these energies.

ACKNOWLEDGMENTS

I wish to express my appreciation to the many people of the Lawrence Radiation Laboratory who have aided me in this work.

I take especially great pleasure in thanking Professor Burton J. Moyer for his continued interest and counsel throughout the course of my research studies. I am also indebted to Dr. Robert W. Kenney for his advice and supervision in all phases of this work.

I owe much to my co-worker, Mr. Paul G. M. McManigal for his invaluable assistance, advice, and support in all aspects of this experiment. To him I express my sincere gratitude and thanks.

I am greatly indebted to Dr. Thomas J. Devlin for the use of his talents as a physicist with extensive knowledge of computer techniques in helping me develop an efficient and versatile method of data reduction.

I wish to thank Dr. Robert J. Cence for his helpful advice during the analysis of the data, and for the use of his phase-shift-search computer programs.

Of special mention is the invaluable assistance of Dr. Jerome A. Helland in the setting up of the experiment. His complete cooperation in the simultaneous use of the pion beam is gratefully acknowledged.

For their diligent efforts and skill during the rigors of a Bevatron experiment, many thanks are due to Mr. Philip M. Ogden and Mr. Donald L. Lind.

The enthusiasm and ability of the scanning group have contributed decisively to the successful completion of the experiment. I especially thank Mr. Jay Spoonheim for his invaluable suggestions as to scanning method and data-reduction procedure, as well as for his valuable assistance in the preparing and running of this experiment.

I wish to thank Mr. Leo Leidy for the building and adapting of special equipment used in this experiment, and Miss Miriam L. Machlis for her willing cooperation and able secretarial assistance in putting the presentation of this work in its final form.

The assistance of the Bevatron operating crew, the computer center, and all the scientific research support groups at the Lawrence Radiation Laboratory is gratefully acknowledged.

Finally, I owe my greatest debt of gratitude to my mother, Mrs. Olga C. Eandi, who, having been widowed early in my life, has still managed to give to each of her children the best possible education for his chosen state in life. The value of her continuous encouragement and support throughout my student life is inestimable.

APPENDICES

A. Derivation of Polarization Formulas

Since p-C and πp scattering are both interactions between spin-1/2 and spin-0 particles, a description of these two processes in terms of scattering amplitudes is formally identical.[35] The asymptotic stationary-state wave function describing elastic scattering—involving a spin-1/2 particle and a spin-0 particle—may be written

$$\psi \to e^{ikz} \chi_i + \psi_f(\theta, \phi) \frac{e^{ikr}}{r}, \qquad (A-1)$$

where the scattering amplitude $\psi_f(\theta, \phi)$ may be written as a scattering matrix M operating on the initial spin state:

$$\psi_f(\theta, \phi) = M(\theta, \phi)\chi_i,$$

where M expresses the amplitude of any outgoing spin and momentum state as a function of the incident spin and momentum. Since M is a scalar it must be invariant to space rotations and reflections (parity). For spin-half particles incident on spin-zero particles the most general, nonrelativistic scalar that can be formed is

$$M = f(\theta) + ig(\theta)\, \underset{\sim}{\sigma} \cdot \underset{\sim}{n}, \qquad (A-2)$$

where θ is the scattering angle in the c.m., $\underset{\sim}{\sigma}$ is the Pauli spin operator for spin-1/2, $\underset{\sim}{n}$ is the normal to the scattering plane (a unit vector in the direction of $\underset{\sim}{k}_i \times \underset{\sim}{k}_f$), and f and g are the so-called "non-spin flip" and "spin-flip" scattering amplitudes, respectively.

Now, for a polarized incident beam the differential cross section can be written as

$$I = \frac{(\psi_f^\dagger, \psi_f)}{(\chi_i^\dagger, \chi_i)} = (\chi_i^\dagger, M^\dagger, M\chi_i)$$

$$= |f|^2 + |g|^2 + 2 \operatorname{Im} f^* g \, \underset{\sim}{P}_i \cdot \underset{\sim}{n}, \qquad (A-3)$$

where $\underset{\sim}{P}_i = (\chi_i, \underset{\sim}{\sigma} \chi_i)$ is the polarization of the incident beam.

The polarization after scattering from the spin-0 target is given by

$$P_f = \frac{(\psi_f^\dagger, \sigma \, \psi_f)}{(\psi_f, \psi_f)} \tag{A-4}$$

$$= \frac{1}{I}\left\{\left(|f|^2 - |g|^2\right)P_i + \left[2|g|^2(P_i \cdot n)n\right] + \left(2 \, \text{Re} \, f^* g \, P_i \times n\right) + \left(2 \, \text{Im} \, f^* g \, n\right)\right\},$$

where the following relations have been used:

$$\sigma(\sigma \cdot n) = i \, n \times \sigma + n,$$

$$(\sigma \cdot n)\sigma = -i \, n \times \sigma + n,$$

$$(\sigma \cdot n) \, \sigma(\sigma \cdot n) = 2(\sigma \cdot n)n - \sigma.$$

1. Pion-proton scattering

In this case the protons are initially unpolarized, so that $P_i = 0$. Then from Eq. (A-3)

$$I = |f|^2 + |g|^2 = I_0, \tag{A-5}$$

and from Eq. (A-4)

$$P_f = \frac{2 \, \text{Im} \, f^* g}{I_0} \, n. \tag{A-6}$$

Since the scattering amplitudes $f(\theta)$ and $g(\theta)$, which characterize the interaction, are complex numbers and vary with scattering angle and energy, the recoil protons will in general be polarized. Also, since we are scattering an unpolarized beam (pions) from an un-polarized-proton target, the direction of the polarization of the recoil protons is normal to the plane of scattering. This is so because the polarization, being an axial vector, must necessarily be parallel to the only axial vector defined in the primary collision, namely, the vector cross product of the initial and final momentum for either pion or proton.

2. Polarized proton-carbon scattering

For a polarized incident beam of polarization P_i we have from Eqs. (A-3) and (A-5)

$$I = I_0(1 + \underset{\sim}{A} \cdot \underset{\sim}{P}_i) = I_0(1 + P_i A \cos \phi), \qquad (A-7)$$

where $\underset{\sim}{A} = A\underset{\sim}{n} = \dfrac{2 \operatorname{Im} f^* g}{I_0} \underset{\sim}{n}$ is a property of the carbon and the energy and angle of scattering, and ϕ is the angle between the incident polarization direction and the normal to the p-C scattering plane.

If we introduce the scattering asymmetry

$$\epsilon = \frac{I(\phi) - I(\phi + \pi)}{I(\phi) + I(\phi + \pi)} = P_i A(E, \theta) \cos \phi, \qquad (A-8)$$

then it is clear that the polarization of nucleon beams can be detected by the scattering from a complex nucleus like carbon, which shows asymmetries proportional to the polarization of the beam. This proportionality constant is defined as the analyzing power $A(E, \theta) \cos \phi$.

B. Partial Wave Analysis

The data obtained in $\pi^\pm p$ scattering experiments can be analyzed by the method of partial waves.[36] In this type of analysis the quantum-mechanical wave function [Appendix A, Eq. (A-1)] is expanded in terms of eigenfunctions of definite orbital angular momentum. In doing this, we have a representation in which the S-matrix is diagonal, and therefore only multiplies the components of the expanded wave function with a factor $e^{2i\Delta}$, where Δ is the so-called phase shift for that particular angular momentum state. Thus, in a well-known fashion, the coherent amplitude $f(\theta)$ and the spin-flip amplitude $g(\theta)$ defined in Appendix A, Eq. (2) are given by

$$f(\theta) = \lambda \sum_\ell \left[(\ell + 1) A_{\ell+} + \ell A_{\ell-} \right] P_\ell(\cos \theta), \qquad (B-1)$$

$$g(\theta) = \lambda \sum_\ell \left[A_{\ell-} - A_{\ell+} \right] \sin \theta \frac{d}{d(\cos \theta)} P_\ell(\cos \theta), \qquad (B-2)$$

where $A_{\ell\pm}$ is the scattering amplitude for the $\ell = J \mp 1/2$ and is related to the S-matrix diagonal element $e^{2i\Delta_{\ell\pm}}$ (by imposing the unitary condition) through the relation

$$A_{\ell\pm} = \frac{e^{i2\Delta_{\ell\pm}} - 1}{2i} \qquad . \qquad \text{(B-3)}$$

In the energy region of this experiment, absorption processes are important and can be included by allowing the phase shifts $\Delta_{\ell\pm}$ to become complex:

$$\Delta_{\ell\pm} = \delta_{\ell\pm} + i\gamma_{\ell\pm} ;$$

making $S_{\ell\pm} = \eta_{\ell\pm} e^{2i\delta_{\ell\pm}}$, where $\eta_{\ell\pm} = e^{-\gamma_{\ell\pm}}$ is the absorption parameter. For elastic scattering $\eta_{\ell\pm} = 1$.

In terms of these partial amplitudes $A_{\ell\pm}$, the total cross section σ_T, the real part of the forward scattering amplitude $D(0)$, the differential cross section $d\sigma/d\Omega$, and polarization P are given by

$$D(0) + i \frac{\sigma_T}{4\pi\lambda} = \lambda \sum_{\ell} \left[(\ell + 1) A_{\ell+} + \ell A_{\ell-} \right], \qquad \text{(B-4)}$$

$$\frac{d\sigma}{d\Omega} = |f|^2 + |g|^2 = \sum_{n=0}^{2\ell_{max}} a_n \cos^n\theta, \qquad \text{(B-5)}$$

$$P \frac{d\sigma}{d\Omega} = 2\,\text{Im}\,f^* g = \sin\theta \sum_{n=0}^{(2\ell_{max}-1)} b_n \cos^n\theta, \qquad \text{(B-6)}$$

where ℓ_{max} is the highest angular momentum state that can be within the reach of the nuclear force, and

$$a_n = \lambda^2 \sum_{\ell=0}^{\ell max} \sum_{\ell'=0}^{\ell} \sum_{J'=\ell-}^{\ell+} \sum_{J=\ell-}^{\ell+} a(\ell, \ell', J, J'; n) \ \text{Re}\ A^*_{\ell J} A_{\ell' J'},$$

$$\text{(B-7)}$$

$$b_n = \lambdabar^2 \sum_{\ell=0}^{\ell_{max}} \sum_{\ell'=0}^{\ell} \sum_{J'=\ell'}^{\ell'+} \sum_{J=\ell'-}^{\ell+} \beta(\ell, \ell', J, J'; n) \, \text{Im} \, A_{\ell J}^* A_{\ell' J'}) \quad (B-8)$$

where $a(\ell, \ell', J, J'; n)$ and $\beta(\ell, \ell', J, J'; n)$ are real coefficients obtained by algebraically rearranging the above expressions in increasing powers of $\cos \theta$.

In the particular case of $\pi^{\pm} p$ scattering we have three elastic channels open:

$$A_{\ell J}^- \quad \text{for } \pi^- + p \to \pi^- + p,$$

$$A_{\ell J}^0 \quad \text{for } \pi^- + p \to \pi^0 + n,$$

$$A_{\ell J}^+ \quad \text{for } \pi^+ + p \to \pi^+ + p.$$

These three quantities, due to isotopic conservation, can be further decomposed into iso-spin states $I = 3/2$ and $I = 1/2$ as follows:

$$A_{\ell J}^- = \frac{1}{3} A_{\ell J}(3/2) + 2/3 \, A_{\ell J}(1/2),$$

$$A_{\ell J}^0 = \frac{\sqrt{2}}{3} \left[A_{\ell J}(3/2) - A_{\ell J}(1/2) \right],$$

$$A_{\ell J}^+ = A_{\ell J}(3/2).$$

The knowledge of the amplitudes $A_{\ell J}(I)$ completely determines πN scattering.

C. The Maximum Likelihood Method

The maximum likelihood method can be stated as follows:[37, 38]

Let $f[(x_1, x_2, \cdots, x_m)_j; a]$ be a normalized probability distribution of known analytical form for random events that can be described by m random variables and an unknown parameter a. Let successive samples $S_k (k = 1, 2, \cdots)$ be taken, each sample containing n events described by $(x_1, x_2, \cdots, x_m)_j$ where $j = 1, n$. Then if there exists any estimate a^* of the parameter a from the data sample S_k such that the likelihood function, defined as $L(n, k, a) = \prod\limits_{n} f[(x_1, x_2, \cdots, x_m)_j; a]$, satisfies the maximum condition

$$\left[\frac{\partial}{\partial P} \ln L(n, k, a) \right]_{a = a^*} = 0,$$

then the estimate a^* is unique and is the most probable value that can be obtained from the experimental results, $(x_1, x_2, \cdots x_m)_j$, $j = 1, n$.

The relative probabilities of a can be displayed as a plot of $L(n, k, a)$ vs a. The rms spread of a about a^*, Δa, is a conventional measure of the accuracy of the determination of $a = a^*$, where

$$\Delta a = \left[\frac{\int (a - a^*)^2 L(n, k, a) da}{\int L(n, k, a) da} \right]^{1/2}.$$

In general, the likelihood function will be close to a Gaussian distribution (it can be shown to approach a Gaussian as $n \to \infty$), whose variance is estimated from a given sample by

$$\Delta a = -\left\{ \left[\frac{\partial^2 \ln L(n, k, a)}{\partial P^2} \right]_{a = a^*} \right\}^{-1/2}.$$

For a small sample, however, the method provides an estimate of the parameter a but does not give the distribution of the estimate to be expected in successive samples. In such a case it is better to present a plot of $L(n, k, a)$ rather than merely quoting a^* and Δa. The maximum

likelihood theorem, which is proved by Cramer,[38] states that in the limit of large n, a^* approaches the true physical value of the parameter a; and furthermore, there is no other method of estimation that is more accurate.

We can now estimate the value of the parameter P in a sample from the distribution

$$f\,[\,(\theta, \phi, E); P\,] = \eta(\theta, \phi, E)\sigma(\theta, E)\,[1 + P\,A(\theta, E)\cos\phi], \qquad (C\text{-}1)$$

where $\eta(\theta, \phi, E)$ is the detection efficiency, assumed unbiased, $\sigma(\theta, E)$ is the unpolarized cross section, $A(\theta, E)$ is the analyzability, and θ and ϕ are, respectively, the space scattering angle and azimuthal angle between the direction of polarization and the normal to the scattering plane. The logarithm of the likelihood function for a sample of n events $(\theta, \phi, E)_j$, $j = 1, \cdots, n$, is therefore

$$\ln\,L = \sum_{j=1}^{n} \ln\,\eta_j\sigma_j + \sum_{j=1}^{n} (1 + PA_j\cos\phi_j),$$

and the condition for the maximum is obtained by differentiation

$$\left(\frac{\partial}{\partial P}\,\ln\,L\right)_{P = P^*} = \sum_{j=1}^{n}\left(\frac{A_n\cos\phi_j}{1 + P^*A_j\cos\phi_j}\right) = 0.$$

Notice that the unpolarized cross section and the detection efficiency do not appear in this formula. The variance is determined by the next-higher derivative:

$$\Delta P = \left(\frac{\partial^2\ln\,L}{\partial P^2}\right)_{P = P^*}^{1/2} = \left[\sum_{j=1}^{n}\left(\frac{A_j\cos\phi_j}{1 + P^*A_j\cos\phi_j}\right)^2\right]^{-1/2}.$$

If the magnitude of n allows the likelihood function to be nearly
Gaussian so that

$$L \approx \exp\left[-\frac{1}{2}\left(\frac{P - P^*}{\Delta P}\right)^2\right],$$

a good approximation to the variance is given by that increment of P
that reduces the likelihood function by

$$L/L_{max} = e^{-1/2}. \tag{C-2}$$

D. Scanning-Efficiency Formulas

Consider two independent scans of the data in which N_1 events
were found by the first scan and N_2 events were found by the second
scan. Let us define:

n_1 = the number of events found by Scan 1 that were not found
by Scan 2,

n_2 = the number of events found by Scan 2 that were not found
by Scan 1,

$N_c = N_1 - n_1 = N_2 - n_2$ is the number of events by both scans.
Thus the total number of different individual events found by both scans
is $N = N_c + n_1 + n_2$. Suppose the true total number of events (events
both found and not found) is N_t; then we have

$$\begin{align}
N_1 &= \epsilon_1 N_t, \\
N_2 &= \epsilon_2 N_t, \\
N_c &= \epsilon_1 \epsilon_2 N_t,
\end{align} \tag{D-1}$$

where ϵ_1 and ϵ_2 are the scanning efficiencies of Scan 1 and Scan 2,
respectively. Solving for ϵ_1 and ϵ_2 we have

$$\epsilon_1 = \left(1 + \frac{n_2}{N_c}\right)^{-1}, \qquad \epsilon_2 = \left(1 + \frac{n_1}{N_c}\right)^{-1}, \tag{D-2}$$

and the rms statistical uncertainty for the Scan 1 efficiency is

$$\Delta\epsilon_1 = \epsilon_1(1 - \epsilon_1)\left(\frac{1}{n_2} + \frac{1}{N_c}\right)^{1/2}. \tag{D-3}$$

If we further divide the events found in both scans into right and left scatters, we can calculate the efficiency, ϵ_R and ϵ_L, for detecting left and right scatters separately, thus providing a measure of the scanning bias, a, which is defined as

$$a = \frac{\epsilon_R - \epsilon_L}{\epsilon_R + \epsilon_L} \quad , \tag{D-4}$$

and whose error is given by

$$\Delta a = \frac{1 - a^2}{2} \left[\left(\frac{\Delta\epsilon_R}{\epsilon_R} \right)^2 + \left(\frac{\Delta\epsilon_L}{\epsilon_L} \right)^2 \right]^{1/2} \quad . \tag{D-5}$$

REFERENCES

1. G. M. G. Lattes, H. Muirhead, G. P. S. Occhialini, and C. F. Powell, Nature 159, 694 (1947).

2. H. C. Burrows, D. O. Caldwell, D. H. Frisch, D. A. Hill, D. M. Ritson, R. A. Schluter, and M. A. Wahlig, Phys. Rev. Letters 2, 119 (1959).

3. T. J. Devlin, B. J. Moyer, and V. Perez-Mendez, Phys. Rev. 125, 690 (1962).

4. J. C. Brisson, J. F. Detoeuf, P. Falk-Vairant, L. van Rossum, and G. Valladas, Nuovo Cimento 19, 210 (1961).

5. M. Gell-Mann and K. M. Watson, Ann. Rev. Nucl. Sci. 4, 219 (1955).

6. F. P. Dixon and R. L. Walker, Phys. Rev. Letters 1, 149, 458 (1958).

7. J. I. Vette, Phys. Rev. 111, 622 (1958).

8. R. F. Peierls, Phys. Rev. 118, 325 (1960).

9. B. J. Moyer, Rev. Mod. Phys. 33, 367 (1961).

10. J. A. Helland, T. J. Devlin, D. E. Hagge, M. J. Longo, B. J. Moyer, and C. D. Wood, Phys. Rev. Letters 10, 27 (1963).

11. S. Minami, Progr. Theoret. Phys. (Kyoto) 11, 213 (1954).

12. J. J. Sakurai, Phys. Rev. Letters 1, 258 (1958).

13. P. C. Stein, Phys. Rev. Letters 2, 473 (1959).

14. R. Querzoli, G. Salvini, and A. Silverman, Nuovo Cimento 19, 53 (1961).

15. See, for instance, G. Salvini, in Proceedings of the 1960 Annual International Conference on High-Energy Physics at Rochester (Interscience Publishers, Inc., New York, 1960), p. 3.

16. M. J. Moravcsik, Phys. Rev. 118, 1615 (1960).

17. P. B. Shaw, Phys. Rev. 124, 1971 (1961).

18. E. F. Beall, B. Cork, P. G. Murphy, W. A. Wenzel, C. M. P. Johnson, and L. J. Koester, Phys. Rev. 126, 1554 (1962).

19. J. A. Helland, Differential Cross Sections for Elastic Scattering of Positive Pi Mesons on Protons in the Energy Region 500 to 1600 MeV (Ph. D. Thesis) Lawrence Radiation Laboratory Report UCRL-10378, August 1962 (unpublished).

20. Lawrence Radiation Laboratory Counting Handbook, UCRL-3307 Rev., January 1959 (unpublished).

21. Symposium on Spark Chambers, Rev. Sci. Instr. 32, 480-531, (1961).

22. E. F. Beall, B. Cork, P. G. Murphy, and W. A. Wenzel, Nuovo Cimento 20, 520 (1961).

23. Spark Chamber Pulser, Lawrence Radiation Laboratory Engineering Drawing No. 5V2054.

24. Range-Energy Tables by M. Rich and R. Madey, University of California Radiation Laboratory Report, UCRL-2301, March 1954 (unpublished).

25. V. Z. Peterson, Lawrence Radiation Laboratory Report UCRL-10622 (unpublished).

26. J. W. Cronin, Phys. Rev. 118, 824 (1960).

27. P. Cziffra and M. J. Moravcsik, Lawrence Radiation Laboratory Report UCRL-8523 Rev., June 1959 (unpublished).

28. O. T. Vik, Scattering of Negative Pions on Protons at 310 MeV: Recoil-Nucleon Polarization and Phase-Shift Analysis (Ph. D. Thesis), Lawrence Radiation Laboratory Report UCRL-10253, May 1962 (unpublished).

29. R. R. Wilson, Phys. Rev. 110, 1212 (1958).

30. L. F. Landovitz and L. Marshall, Phys. Rev. Letters, 3, 190 (1959).

31. J. A. Helland, T. J. Devlin, D. E. Hagge, M. J. Longo, B. J. Moyer, and C. D. Wood, Lawrence Radiation Laboratory Report UCRL-10478, September 1962 (unpublished).

32. J. Kirz, The Reaction $\pi^- p \to \pi^- \pi^+ n$ Below 800 MeV (Ph. D. Thesis) Lawrence Radiation Laboratory Report UCRL-10720, March 1963 (unpublished).

33. R. F. Peierls, Phys. Rev. Letters 6, 641 (1961).

34. J. S. Ball and W. R. Frazer, Phys. Rev. Letters 7, 204 (1961).

35. W. S. C. Williams, An Introduction to Elementary Particles (Academic Press, Inc., New York, 1961), Chap. VIII.

36. Ibid., Chap. III.

37. J. Orear, University of California Radiation Laboratory Report
UCRL-8417, August 1958 (unpublished).

38. H. Cramér, Mathematical Methods of Statistics (Princeton
University Press, Princeton, New Jersey, 1958), p. 498.